Low-level Z_{DR} Signatures in Supercell Forward Flanks: the Role of Size Sorting and Melting of Hail

Daniel T. Dawson II[1,2,3], Edward R. Mansell[1], Youngsun Jung[3], Louis J. Wicker[1], Matthew R. Kumjian[1,2], and Ming Xue[3]

NOAA/National Severe Storms Laboratory[1]
National Weather Center
120 David L. Boren Blvd.
Norman, OK 73072

Cooperative Institute for Mesoscale Meteorological Studies[2]
National Weather Center
120 David L. Boren Blvd.
Norman, OK 73072

Center for Analysis and Prediction of Storms[3]
University of Oklahoma, Norman Oklahoma 73072

Submitted to *Journal of the Atmospheric Sciences*

Revised submission: April 2013

Corresponding author address and current affiliation: Daniel T. Dawson II, Center for Analysis and Prediction of Storms, 120 David L. Boren Blvd, Norman, OK 73072.
E-mail: ddawson@ou.edu

Abstract

The low levels of supercell forward flanks commonly exhibit distinct differential reflectivity (Z_{DR}) signatures, including the low-Z_{DR} hail signature, and the high-Z_{DR} "arc". The Z_{DR} arc has been previously associated with size sorting of raindrops in the presence of vertical wind shear, and this model is here extended to include size sorting of hail. Idealized simulations of a supercell storm observed by the KOUN polarimetric radar on 1 June 2008 are performed using a multi-moment bulk microphysics scheme, in which size sorting is allowed or disallowed for hydrometeor species. Several velocity-diameter relationships for the hail fall speed are considered, as well as fixed or variable bulk densities that span the graupel-to-hail spectrum. A polarimetric emulator is used to derive polarimetric fields from the hydrometeor state variables.

It is found that size sorting of hail has a strong impact on Z_{DR}, and can result in a Z_{DR} arc from melting hail even when size sorting is disallowed in the rain field. The low-Z_{DR} hail core only appears when size sorting is allowed for hail. The mean storm-relative wind in a deep layer is found to align closely with the gradient in mean mass diameter of both rain and hail, with a slight shift toward the storm-relative mean wind below the melting level in the case of rain. The best comparison with the observed 1 June 2008 observed supercell is obtained when rain and hail are both allowed to sort and the bulk density and associated fall speed curve for hail is predicted by the model microphysics.

1. Introduction

Dual-polarized radars have many advantages over their single-polarized counterparts, particularly an enhanced ability to distinguish between different types, sizes, and shapes of hydrometeors within precipitating systems (Balakrishnan and Zrnic 1990; Herzegh and Jameson 1992; Ryzhkov and Zrnic 1998; Zrnić and Ryzhkov 1999; Straka *et al.* 2000; Bringi and Chandrasekar 2001; Zrnic *et al.* 2001; Ryzhkov *et al.* 2005; Tessendorf *et al.* 2005; Heinselman and Ryzhkov 2006; Park *et al.* 2009) as well as distinguishing between hydrometeors and other non-meteorological scatterers, such as insects, birds, dust, and debris (e.g., Ryzhkov *et al.* 2005; Gourley *et al.* 2007). Several polarimetric variables can be derived from the information provided by the horizontally and vertically polarized beams and their differential interactions with hydrometeors. Among these, the differential reflectivity Z_{DR} (the ratio of radar reflectivity factors at horizontal and vertical polarizations, Seliga and Bringi 1976) is useful for distinguishing between regions of hail and rain. Further, it is substantially positive (depending on the radar wavelength) for rain distributions skewed toward large oblate drops. In combination with other polarimetric variables, Z_{DR} yields much information about the particle (or drop) size distribution (P[D]SD) of rain, which aids in improving radar-derived rain rate relations (e.g., Bringi *et al.* 2004; Giangrande and Ryzhkov 2008) and understanding of microphysical processes and their relationship to the kinematics of storms, which is the subject of the present study.

Among precipitating cloud systems, supercell thunderstorms produce some of the most severe weather on the planet, including large hail, damaging straight-line winds, and tornadoes. Recent studies have shown that supercells systematically display certain (possibly unique) polarimetric signatures, which have yielded significant insight into the complex interplay of kinematics and microphysical processes within these storms (Kumjian and Ryzhkov 2008; Romine *et al.* 2008). One of the most common polarimetric signatures noted is the so-called Z_{DR} "shield" or "arc"[1]. This signature appears within the forward-flank reflectivity region at low levels (below ~1-2 km AGL) and is characterized by significant positive values of Z_{DR} collocated with low-to-moderate reflectivity. Kumjian and Ryzhkov (2009; 2012, hereafter KR09 and KR12, respectively), used a simplified bin sedimentation model to interpret the Z_{DR} arc as a result of enhanced size sorting of rain associated with the strong low-level shear in the inflow environment of the supercell storm, and also demonstrated a positive correlation with the magnitude of the low-level storm relative helicity and the "strength" of the Z_{DR} arc.

KR09 and KR12 limited their investigation to idealized rain shafts with prescribed initial distributions aloft. In typical supercell storms, most of the rain is derived from the melting of ice particles, particularly snow, graupel and hail. Romine et al. (2008), in their study of the 8 May 2003 Oklahoma City tornadic supercell, attributed the source of large drops in the Z_{DR} "shield" as melted graupel. Kumjian et al. (2010, hereafter KRMS10) also explicitly identify the source of rain in the Z_{DR} arc as melted graupel in their study of the 1 June 2008 western Oklahoma nontornadic supercell. Below the melting level, a given area of the precipitation region may include contributions to Z_{DR} from both rain and partially melted graupel or hail. The Z_{DR} signature of the latter can vary significantly depending on the size of the hydrometeors and the amount of water coating. For relatively dry, large, and tumbling hailstones, the Z_{DR} is near 0. At

[1] Whether the Z_{DR} "arc" and "shield" are the same feature or not remains an open question. While this work does not address this question directly, we find it plausible that the Z_{DR} "arc" may be a small-scale enhancement of the Z_{DR} "shield" that may not be explicitly resolved with the resolution of the models used in this study. Future work may address this question.

the other end of the spectrum, small, nearly completely melted hailstones transition to a maximum stable large rain drop (Rasmussen *et al.* 1984, hereafter RLP84), and thus exhibit high Z_{DR}. It remains an open question how much of the low-level (~0-2 km) enhanced Z_{DR} in the forward flanks of supercells can be attributed to melting graupel or hail vs. rain. Other polarimetric variables, such as the cross-correlation coefficient ρ_{HV} and specific differential phase K_{DP}, are also helpful in this regard: the former is sensitive to mixtures of rain and hail and the latter to the presence of liquid water, whether in raindrops or as a shell of liquid water on melting graupel and hail.

A major challenge in numerical modeling of convective storms is the treatment of the rimed ice category or categories (graupel or hail or both), particularly assumptions about the bulk density and fall speeds (e.g., Gilmore *et al.* 2004). The impact of environmental shear on sorting of the graupel and hail fields above the melting level has been relatively unexplored, particularly how it then contributes to shaping the distribution of rain and melting graupel and hail sizes below the melting level, which can modify the observed Z_{DR} there in complex ways. The depth of the shear layer in supercell environments often extends well above the melting level [O(3-5 km)], and thus substantial sorting of graupel and hail may occur long before melting occurs. Motivated by these questions, we investigate the impact of size sorting and melting on the magnitudes of Z_{DR} below the melting level through the use of numerical simulation. Our first approach is to examine 3D idealized numerical simulations of a well-observed supercell: the 1 June 2008 nontornadic supercell that was the subject of KRMS10. We show how the basic polarimetric features (with an emphasis on the Z_{DR} field) in the low levels of the forward flank can be reasonably reproduced by a triple-moment (3M) bulk microphysics scheme, particularly when the bulk density of the rimed ice category is predicted, rather than held fixed as is usually the case. Then, to simplify the analysis and in an attempt to reveal the essential physics, we make use of relatively simple environmental setups that are reminiscent of the steady 3D precipitation shaft experiments of KR09, but include the use of varying fall speed relations for graupel and hail. In both sets of experiments, similar to KR12, we investigate the impact of size sorting by sedimentation and demonstrate the separate impacts of sorting of graupel and hail on hand, and rain on the other, on the low-level Z_{DR} signatures.

This paper is organized as follows. Section 2 describes aspects of the bulk microphysics scheme and the polarimetric emulator used to derive Z_{DR} from the model microphysics fields. Sections 3 and 4 describe the methodology and results of the supercell simulation experiments and 3D precipitation shaft experiments, respectively. Finally section 5 summarizes the paper, and discusses questions to guide future work.

2. Microphysics Scheme and Polarimetric Emulator

a. Microphysics scheme

The microphysics scheme used in this study is an upgraded version of the multi-moment (MM) scheme described in Mansell et al. (2010, hereafter MZB10), developed at NSSL, which itself is based on an earlier scheme of Ziegler (1985). The full scheme allows for multiple options at runtime to control various microphysical processes and levels of complexity, such as the number of moments predicted, whether only one rimed ice category (graupel or hail, depending on density and fall speed assumptions), or two (graupel and hail) are included, and whether the bulk densities of graupel and hail are allowed to vary, among others. Up to three moments of the gamma size distribution are predicted for graupel, hail and rain, the 0^{th}, 3^{rd}, and 6^{th} moments, following the approach of Milbrandt and Yau (2005b, hereafter MY05b), but only the first two moments for the remaining species. The closure scheme for the *Z* rate equations mainly follows the approach of MY05b (see Appendix A), and the reader is otherwise referred to MZB10 for a description of the microphysics scheme. In the current study, we utilize only one rimed ice category in any given simulation for the bulk of the experiments. However, since the variation of the fall speeds with density can be substantial, we investigate the impact of maintaining fixed bulk densities for rimed ice of 500 kg m^{-3} (graupel) and 900 kg m^{-3} (hail), respectively on the one hand, and allowing the rimed ice category to vary in density (a spectrum of graupel-to-hail), as in MZB10. For convenience, throughout the paper, when using fixed bulk densities, the term "graupel" will be used for the low-density (500 kg m^{-3}) slower-falling case, while the term "hail" will be used for the high-density (900 kg m^{-3}) faster-falling case. In the variable-density experiments, the term "hail" will be used, mainly because, as will be seen, the density and fall speeds have already risen to the "hail-like" part of the spectrum by the time the hydrometeors have fallen much below the melting level owing to the increase in density during melting. These configurations of the scheme will be referred to throughout the rest of the paper as the "NFD" and "NVD" schemes (for NSSL Fixed Density and NSSL Variable Density, respectively, after Yussouf *et al.* 2013).

A quantity that will be used throughout this paper is the mean mass (or volume) diameter D_m, which is defined as

$$D_m = \left[\frac{6\rho_a q_x}{\pi \rho_x N_{T,x}}\right]^{1/3}, \tag{1}$$

where ρ_a is the air density, q_x is the mass mixing ratio (the subscript x refers to any given hydrometeor category), ρ_x is the bulk hydrometeor density, and $N_{T,x}$ is the total number concentration. This form of D_m is valid for constant density spheres. As described in (Milbrandt and Yau 2005a, hereafter MY05a), this quantity serves as a proxy for the amount of size sorting that has occurred in the hydrometeor distribution, when compared to its initial value aloft.

Physically speaking, D_m represents the diameter of the particle whose mass is equal to that of the mean mass of the distribution.

The terminal velocity of graupel and hail is assumed to follow a power law with respect to diameter of the form $v(D) = \gamma a D^b$, where a and b are typically empirically derived constants, and $\gamma = \left(\frac{\rho_0}{\rho_a}\right)^{0.5}$ is the density correction factor, where ρ_0= 1.204 kg m^{-3} and ρ_a is the air density. The power law relationships used in this study are summarized in Fig. 1 and Table 1. The labels A,B,C, and D in Fig. 1 are used in the experiment naming nomenclature to be discussed later in the paper. Curves A and B are derived from the terminal velocity relation for graupel and hail as used in Wisner et al. (1972) and adopted by MZB10. They depend on the assumed hydrometeor bulk density and drag coefficient, with increasing terminal fall speeds for all diameters as the bulk density increases. Thus curve A represents graupel with a fixed density of 500 kg m^{-3} and likewise curve B for hail (900 kg m^{-3}). Curves C and D are from Ferrier (1994) for graupel and hail, respectively. When graupel and hail are allowed to vary in density, the resulting fall speed curves lie between the lowest density (170 kg m^{-3}) curve and the high-density curve (lower and upper black dashed lines in Fig. 1, respectively). This variability in the assumed fall speed relations has consequences for the distribution of graupel and hail (also noted explictly by Milbrandt and Morrison 2013) and on the distribution of Z_{DR} in the simulations in this study.

Several recent studies (Wacker and Seifert 2001; Dawson *et al.* 2010; Mansell 2010; Milbrandt and McTaggart-Cowan 2010; KR12) have demonstrated the following characteristics of typical bulk microphysics schemes in regards to the size-sorting process: 1) single-moment (1M) schemes are incapable of parameterizing size sorting (Dawson *et al.* 2010), 2) double-moment (2M) schemes without a correction mechanism (e.g., Mansell 2010) or diagnostic formula for the gamma shape parameter (MY05a; Milbrandt and McTaggart-Cowan 2010) grossly overestimate size-sorting, and 3) Triple-moment (3M) schemes are able to closely approximate an analytical bin solution for pure sedimentation (MY05a, Milbrandt and McTaggart-Cowan 2010, KR12). The lack of size sorting in a 1M scheme is a consequence of the use of a single predicted variable (q, the total mass), from which all other PSD-related variables (including D_m) are diagnosed. In contrast, the size-sorting mechanism in a MM bulk scheme works by allowing each predicted moment of the size distribution to sediment at its own moment-weighted fall speed, such that mean size can evolve independently of total mass. For a 2M scheme that predicts N_t and q, the mass-weighted fall speed is greater than the number-weighted fall speed, allowing more q to reach lower levels faster than N_t, increasing D_m toward the ground (MY05a). Similarly, in a triple-moment (3M) scheme that predicts N_t, q, and Z, the reflectivity-weighted fall speed is generally greater than the mass-weighted fall speed, resulting in an increase of the shape parameter (α in Eq. A1) in the gamma distribution during size sorting. A larger shape parameter narrows the size distribution and limits further size sorting by causing the weighted fall speeds to be closer in value. A 2M scheme does not have this feedback, and can exhibit unrealistically large D_m during the size-sorting process unless mitigating steps are taken (e.g., MY05a, Mansell 2010).

Therefore, in the context of MM bulk schemes a 3M scheme is the most appropriate for studying polarimetric radar signatures that depend on size sorting effects. For this reason, we utilize the 3M version of the NFD and NVD scheme for the experiments in this study, but we alternately enable or disable size sorting by either allowing all predicted moments to sediment at their appropriately-weighted fall speed (hereafter, the “3M” experiments), or by forcing all three predicted moments to instead sediment at the mass-weighted fall speed, effectively making the *process of sedimentation only* 1M for these experiments (hereafter, the "1M" experiments). We emphasize however, that in *all experiments* all other processes are still fully 3M, and all three moments are tracked independently in the model.

b. Polarimetric emulator

To derive polarimetric fields from the model hydrometeor fields, we employ a modified version of the polarimetric emulator of Jung et al. (2010, hereafter JXZ10). In what follows, we stress that the emulator is applied to the model hydrometeor fields entirely "offline". That is, no feedback from the emulator is provided to the model; it is an entirely diagnostic procedure. The JXZ10 emulator uses the T-matrix method (Waterman 1969; Vivekanandan *et al.* 1991; Mishchenko 2000) to create scattering amplitude look-up tables for all hydrometeor categories as a function of particle diameter and assumed liquid water fraction in the case of the ice categories. The emulator can accommodate radar wavelengths at X-, C-, and S-bands, but we examine only the S-band case in this study, since the KOUN radar with which comparisons are made is S band. The hydrometeor PSD moments from the model output are used to derive the intercept, shape, and slope parameters for the assumed gamma distribution. Then, for each hydrometeor category, the emulator discretizes the distribution by computing the number concentration in equally spaced equivolume diameter bins from the model PSD at each grid point. Although the model hydrometeor distributions assume spherical particles, the emulator allows for variable axis ratios as a function of diameter for the purposes of the scattering amplitude calculations. To account for wet surfaces on snow, graupel, and hail for the schemes that do not explicitly predict it, the emulator employs a diagnostic method whereby a mixture of the rain and ice fields is used to derive a water fraction on melting ice.

Improvements were made to the JXZ10 emulator for the purposes of this study. The changes mainly concern how small to medium sized ($D \leq$ ~2 cm) hail particles are treated under conditions of melting or wet growth, and how the diagnosed water fraction is applied across the hail distribution. JXZ10 specified a fixed axis ratio for hailstones of all diameters of 0.75, regardless of assumed liquid fraction, although they did provide for a decrease in the standard deviation of the canting angle with increasing liquid fraction, to account for the stabilization effects of the liquid water torus (RLP84). The laboratory investigations of RLP84, however, indicate that initially spherical hailstones of D = ~1.5 cm or less decrease rapidly in axis ratio as they melt due to the buildup of a horizontal water torus, transitioning toward the equilibrium shape of a large ~8 mm raindrop, with an axis ratio of ~0.55. Kumjian and Ryzhkov (2008) pointed out that these "small, wet hailstones are sensed as giant raindrops, characterized by very high Z_{DR}". Borowska et al. (2010) and Ryzhkov et al. (2011) accounted for these characteristics of melting hail in their polarimetric emulator by utilizing linear approximations between the aspect ratio of a dry hailstone and that of a raindrop into which it eventually melts, based on the laboratory investigations of RLP84, and by decreasing the width of the canting angle distribution from 40-50° for dry hail to 10° for completely melted hail. In our study, we follow an approach very similar to that of Ryzhkov et al. (2011) for computing the aspect ratio and width of the canting angle distribution for melting hail with the following main differences: 1) the linear decrease of the canting angle distribution width is applied for water fractions between 0 and 0.5, and is set to 0° above that threshold, and 2) a value of 60° is used for completely dry hail. Finally, we note that the Z_{DR} of melting hail will vary with different assumptions about axis ratios and width of the canting angle distribution, particularly the latter. We performed several tests (not shown) in which these parameters were varied over reasonable ranges and found that the *qualitative* natures of the signatures were not altered. We leave further investigation of this issue to future work.

The water fraction is diagnosed via an iterative method. As a first guess, liquid water is "borrowed" from the q_r field and added to the q_h field (in the more general case of multiple ice species at a point, the rainwater is distributed amongst the different species weighted by their fraction of the total ice mass), up to a maximum of 90% of the rain (to avoid complete depletion of the existing rain field, which is done only for computational convenience). Rasmussen and Heymsfield (1987) developed a formula for the maximum water mass M_w that can exist on a melting hailstone with ice core mass M_i (see their equation 6), and is shown in Fig. 2 along with corresponding axis ratios and canting angle widths at maximum water fraction used in the emulator.

The critical water mass, expressed as a function of the total mass of the melting hailstone M_t (where the masses are in kg), is given by:

$$M_w = 2.51\times10^{-4} + 0.1220 M_t\,, \tag{2}$$

We integrate (2) over the entire (discretized) distribution of the melting hail to determine the maximum water fraction allowed for the entire distribution, denoted $F_{wcrit} = M_w/(M_w + M_i)$. For the case that the available water from the rain exceeds F_{wcrit}, the computed F_{wcrit} is used as the next guess and the process is iterated until convergence, yielding the final diagnosed water fraction F_w. Otherwise, the original first guess is used for F_w. The total number concentrations of both rain and hail are adjusted during this process to preserve the mean mass diameter.

After F_w for the hail distribution is determined, this available liquid water is then distributed amongst the discrete size bins of hail ($F_{w,i}$, i = 1,N_{bin}, where N_{bin} is the number of discrete bins) in the following manner: 1) for hail diameter $D_h \leq 8$ mm, the hailstone is assumed to be completely melted and the water mass is added back to the equivalent rain bins 2) for $D_h >$ 8 mm M_w from (2) is computed and multiplied by the ratio $R_{crit} = F_w / F_{wcrit}$. The former is performed to ensure the emulator treats this portion of the wet graupel and hail spectrum as rain, while the latter ensures that the remaining water fraction is distributed across all (discrete) hail sizes. Thus, our diagnostic water fraction approach differs from that of JXZ08 by allowing $F_{w,i}$ to vary in a physically consistent manner across the graupel and hail size distribution, instead of assuming a constant F_w for each bin. To summarize, the diagnostic water fraction technique takes water from the rain field at a given grid point and applies it to the graupel and/or hail distribution up to either 90% of the rain water available, or to the total amount the distribution can "hold", based on (2), whichever is less.

3. 1 June 2008 Supercell Experiments

a. Methodology

The 1 June 2008 western OK nontornadic supercell was well observed by the KOUN S-band dual-polarized radar; its polarimetric signatures were previously documented by KRMS10, making it a case well suited for our purposes. We perform a series of idealized simulations using a single sounding environment described by a RUC analysis point proximity sounding valid 0100 UTC 1 June 2008 (Fig. 3). The overall supercell (SC) simulation naming convention is patterned after the template SC#R#[Y][X], where the # represents the number of moment-weighted fall speeds used for sedimentation of rain (R) and graupel, hail, or both (Y=G,H,GH), respectively, and X=A,B,C,D, or VD (i.e. indicating either one of the fixed bulk densities and fall speeds in Fig. 1 or variable density and fall speed are used for graupel or hail). All simulations discussed in this section are summarized in Table 2 and details are described in Table 3. We will first examine the results of the "reference" experiment SC3R3HVD (3M sedimentation with variable density graupel/hail). We then focus on two sets of experiments. The first set is designed to test the impact of varying fall speeds and bulk densities for the rimed ice category, over the range of curves shown in Fig. 1, with each experiment using a fixed fall speed curve and bulk density. The second set of experiments is designed to test the impact of size sorting of rain and graupel/hail by systematically allowing (3M sedimentation) or disallowing (1M sedimentation) size sorting in one or both categories. We present results at 70 min of simulation time, roughly midway between the decay of the initial convective pulse and the beginning of the decay phase of the storm, when the storm exhibited quasi-steady classic supercell structure similar to the observations (Fig. 4). Other times during the mature stage of the supercell (not shown) exhibit qualitatively similar structure.

b. Results of reference experiment

We first present results of the reference experiment (SC3R3HVD) and compare with the observed supercell. Fields of Z, Z_{DR}, K_{DP}, and ρ_{HV} are shown in Fig. 4 for the observed supercell and corresponding plots for experiment SC3R3HVD at 932 m AGL and 70 min. The simulation and observations exhibit generally good qualitative agreement in the low-level polarimetric signatures. Visible in both the observed and modeled storm is a low-Z_{DR} (Z_{DR} < ~ 2 dB) hail signature (hereafter the "hail core") in the core of the storm just NE of the hook echo (Fig. 4c,d). The modeled storm Z_{DR} magnitudes (~ 1-1.5 dB) are somewhat higher than the observed (~ 0 dB) in this region. Potential reasons for this discrepancy, all of which involve substantial uncertainty, include 1) the hail diameters may be under-predicted, 2) the observed Z_{DR} could be negatively affected by differential attenuation or nonuniform beamfilling, 3) as previously mentioned, the assumed canting angle distribution width may be inaccurate, or 4) the assumed hail axis ratios may be inaccurate. A thorough investigation of these important issues is left to future work. A

Z_{DR} arc is also apparent on the south edge of the forward flank in both the observed and modeled storms (Fig. 4c,d), although the magnitude of Z_{DR} in the arc is O(1 dB) lower in the simulation than in the observations (4.5-5 dB vs. 5-5.5 dB). In addition, a secondary enhancement (relative to the surroundings) of Z_{DR} ~ 4 dB is apparent in both the observed and modeled storms on the north side of the hail core, running roughly parallel to the Z_{DR} arc, which join together to the east in the forward flank. By examining the rain and hail mean volume diameters, along with the diagnosed water fraction on hail (Fig. 5), we can see that the Z_{DR} arc is in a region dominated by relatively large rain and similarly-sized partially-melted hail, while the hail core is indeed dominated by relatively large and dry hail.

Turning to the K_{DP} field (Fig. 4e,f), while the observations appear to be suffering from nonuniform beam filling problems in the core of the storm (near -112,50 km in Fig. 4e), outside of this region the K_{DP} values and distribution in the forward flank are very similar to the simulation, with the highest K_{DP} values (> 6 deg km^{-1}) found along the major axis of the forward flank in both cases. In the observed storm, regions of relatively low ρ_{HV} (Fig. 4g) are found juxtaposed, as expected, with low Z_{DR} in the hail core (c.f. Fig. 4c), consistent with relatively large, dry, tumbling hailstones. In addition, a close examination of the ρ_{HV} field as one moves ESE down the forward flank near the edge, shows there are still regions of moderately low ρ_{HV} (~0.95) that are collocated with high Z_{DR} associated with the Z_{DR} arc, again, in both the simulation and observations. This suggests that at least part of the observed Z_{DR} arc at this level contains a mixture of partially melted small graupel or hail and large rain, since pure rain would be expected to have ρ_{HV} ~ 1. A similar region of lower ρ_{HV} overlapping the Z_{DR} arc region can be seen in the simulation (Fig. 4h), again in a region of relatively large rain and similarly-sized partially-melted hail (Fig. 5).

However, in SC3R3HVD, ρ_{HV} magnitudes are overall higher than the observations (Fig. 4h), suggesting that the model and/or polarimetric emulator is not capturing enough of the diversity in hydrometeor type or behavior. To test this from the model side, we performed another simulation, SC3R3GHVD, which is similar to SC3R3GVD but with both the graupel and hail categories included (hence the "GH" in the name). Again, we present plots of Z,Z_{DR},K_{DP}, and ρ_{HV} for this simulation in Fig. 6. The addition of the separate hail category has a substantial effect on ρ_{HV}, namely, lowering it to values near 0.9 in the core, closer to the observations. This can be explained simply by the added diversity in hail sizes, water fractions, and assumed tumbling characteristics by allowing two separate rimed ice distributions to exist at a given grid point. In addition, the region of highest Z_{DR} (> 4.5 dB) in the Z_{DR} arc is reduced in size from SC3R3HVD and its orientation better approximates the observed orientation. The magnitudes of Z_{DR} in the hail core are reduced to ~0.5 dB, again closer to the observations (c.f. Fig. 4c). On the other hand, reflectivity magnitudes in the core are over-predicted (> 70 dB), possibly due to an over-prediction of hail diameters or mass mixing ratio (not shown). Testing this hypothesis is difficult, however, without direct observations of hail size distributions and precipitation rates in this case and others. In any case, a clear trend toward an improved polarimetric representation in the simulated supercell is seen when the number of rimed ice categories is increased from one to two.

c. Results of experiments varying bulk graupel/hail density and fall speeds

To better assess the sensitivity of the low-level polarimetric features to the nature of the rimed ice category, we next investigate the impact of a fixed density for the rimed ice category and varying the fall speed relations between the four labeled curves in Fig. 1. (experiments SC3R3YX, where Y=G,H, and X = A,B,C, or D). Neglecting the variation in density and associated fall speed for the rimed ice category results in degraded reflectivity structure and in particular Z_{DR} signatures (Fig. 7) as compared with SC3R3HVD and the observed storm (c.f. Fig 4). For the purposes of this discussion we will mainly be focusing on the Z_{DR} field. Overall, experiment SC3R3HB (Fig. 7c,d) compares most favorably to SC3R3HVD (c.f. Fig. 4), due to the relatively high assumed fixed density (900 kg m^{-3}) and fall speeds in these experiment, which are similar to the predicted bulk density in SC3R3HVD at this level (not shown). The magnitudes of Z_{DR} in the arc with fall speed A (SC3R3GA, Fig. 7b) are substantially reduced relative to that of SC3R3HVD (c.f. Fig. 4), due to the presence of relatively dry, large graupel (Fig. 8b, D_{mg} ~ 8-12 mm) where SC3R3HVD instead has relatively wet, smaller hail (Fig. 5b, D_{mh} ~ 5-6 mm). This difference is a consequence of the relatively low fixed density assumed (500 kg m^{-3}) which results in larger D_{mg} for the same mass mixing ratio, as well as the lower fall speeds relative to SC3R3HVD and more downstream transport for a given D_{mg}. The larger D_{mg} also causes less water to be diagnosed on the graupel surface (Fig. 9a), and results in lower Z_{DR}. In keeping with this trend, fall speed C (SC3R3GC) exhibits an unrealistically large forward flank region with a Z_{DR} arc that is “smeared” over a large east-to-west extent as compared with the observations (c.f. Fig. 4b). Again, this result is a consequence of the even lower fall speeds for graupel assumed in this experiment (c.f. curve “C” in Fig. 1). The relatively slow increase of V_{tg} with diameter for this curve also means that less size sorting can occur over a given range of graupel diameters and explains the relatively broad gradients in D_{mg} (Fig. 8f). Finally, experiment SC3R3HD exhibits Z_{DR} signatures somewhat intermediate between the low-density slow-falling graupel experiment (SC3R3GA) and the high-density, fast-falling hail experiment (SC3R3HB), again due to lower fall speeds assumed (compare curve “D” to curve “B” in Fig. 1).

To summarize, the choice of the fall speed curve and bulk density for graupel or hail has a profound impact on the resulting low-level polarimetric signatures in the simulated supercell: the higher-density, faster-falling hail-like species generally result in polarimetric signatures which are closer to the observed polarimetric observations than the lower-density, slower-falling graupel-like species, when compared to the variable density reference simulation and the observed supercell signatures.

d. Results of size-sorting experiments

Next we examine the experiment sets that use either a single (1) mass-weighted fall speed for sedimentation (i.e., size-sorting disabled) or the three (3) appropriately-weighted fall speeds (i.e., size-sorting enabled, as in SC3R3HVD). In general, as one goes from disallowing size sorting completely (SC1R1HVD, first row in Figs. 10-12) to allowing it for both rain and hail (SC3R3HVD, last row in Figs. 10-12, there is a substantial improvement in the fidelity of the Z_{DR} signatures (Fig. 10 right column) as compared with observations (c.f. Fig. 4, left column). In contrast, the reflectivity structure (Fig. 10 left column) and K_{DP} fields (Fig. 11, left column) are relatively insensitive to these changes across experiments. Z_{DR} does not depend directly on the total hydrometeor mass at a given grid point, but does strongly depend on hydrometeor properties (such as oblateness or tumbling characteristics) that themselves depend on the PSD. In contrast both Z and K_{DP} do depend on total hydrometeor mass (as well as the PSD). This additional dependence on hydrometeor mass may help explain the overall lack of sensitivity (especially in K_{DP}) to size sorting, which strongly modifies the PSD.

The two experiments that disallow sorting in the hail field (SC1R1HVD and SC3R1HVD, first two rows in Figs. 10-12) exhibit relatively poor agreement in the Z_{DR} field with the observed structure, with broad, relatively weak gradients in Z_{DR} over most of the forward flank (Fig.

10b,d), and little evidence of an enhanced Z_{DR} arc or low Z_{DR} hail core. In addition, the ρ_{HV} field displays a broader region of magnitudes < 1 than the other experiments (compare Fig. 11b,d with Fig. 11f,h), which is due to the broader region of (relatively small) graupel in the forward flank. The former is reflected in the D_{mh} field in both experiments (Fig. 12b,d), which displays relatively small values (2-4 mm, close to the average value aloft, not shown) and weak gradients. In SC3R1HVD, the effects of rain sorting are evident with a general south-to-north decrease in D_{mr} in the forward flank (Fig. 12c), but this has little overall impact on the Z_{DR} field, likely due to the contribution from hail. In contrast, SC1R3HVD (Figs. 10-12 third row) is very similar to the reference simulation SC3R3HVD (Fig. 10-12 last row) in regards to the presentation of the Z_{DR} arc and low Z_{DR} hail signature, and both compare favorably to observations (c.f. Fig. 4c). The ρ_{HV} in the hail core in these simulations (Fig. 11f,h) is also lowered relative to the no-hail-sorting runs (Fig. 11b,d), in closer agreement with observations (Fig. 4g). Even though the rain field is not allowed to sort in SC1R3HVD, the pattern of D_{mr} between these latter two experiments is remarkably similar (Fig. 12e,g). This strongly suggests that sorting in the hail field is the dominant factor in controlling the location of the largest rain drops and associated polarimetric radar presentation, at least in regards to the Z_{DR} arc and Z_{DR} hail core signature. Z_{DR} (Fig. 10f) is somewhat over-predicted, however, on the northwest flank of the storm as compared with both SC3R3HVD (Fig. 10h) and the observations (Fig. 4c). This result is reflected in the D_{mr} field, which shows larger D_{mr} in this region in SC1R3HVD (Fig. 12e) than in SC3R3HVD (Fig. 12g). Thus, while size sorting in the graupel and/or hail category appears most important in regards to the two main signatures of interest to this study, there is a noticeable impact from rain sorting as well in the overall Z_{DR} presentation. Finally, we again note that in both SC1R3HVD and SC3R3HVD, a secondary region of enhanced Z_{DR} (relative to the surroundings) north and northeast of the hail core is evident. This signature is a result of a mixture of relatively small, partially melted hailstones that have "sorted out" on the north side of the hail core and relatively large raindrops. This northern enhancement of Z_{DR} can be viewed as representing a transition zone between the relatively large, dry hail to its immediate south and progressively smaller raindrops and completely melted hailstones to its north.

4. 3D Sedimentation Experiments

a. Methodology

Although the impact of size sorting of rain and graupel/hail on forward flank polarimetric signatures is evident in the full supercell experiments, we can investigate their impacts in a more simplified framework that better reveals the underlying physics. To this end, we perform four idealized experiments--mirroring those of the size-sorting supercell experiments above--wherein a constant hail source at the top boundary (set at 12 km AGL) is imposed, and the hail falls and melts in the same horizontally-homogeneous background wind and thermodynamic profile as used for the supercell experiments (Fig. 3). These experiments are identified by the naming template 3D#R#HVD with otherwise the same convention as used previously, and are summarized in Table 4. Horizontal and vertical grid spacings are constant at 500 m and 200 m. Based on the reference supercell experiment (SC3R3HVD), we impose a constant circular source region of hail at the 12 km level utilizing a cosine-squared function for q_h, with a maximum of 8 g kg^{-1} in the center. The mean volume diameter D_{mh} is set to a constant 2 mm, the gamma shape parameter is set to zero, and the initial bulk density is set to 800 kg m^{-3}. The top boundary source region is assumed to be moving with the same speed and direction as the simulated supercell (black star in Fig. 3). While the hail is allowed to fall and melt into rain, for simplicity no dynamic or thermodynamic feedback to the environment is allowed. The simulations are run out to 1800 s, which was found to be sufficient to reach a steady state in all cases. Our goal is to produce a simplified model of the forward flank precipitation region of supercells removed from the main updraft, in which vertical motions play a relatively minor role, and sedimentation and melting of hail into rain in the presence of substantial environmental wind shear are presumably the most important microphysical processes.

We emphasize here that we do not wish to discount the importance of size sorting by the storm updraft *in the region of the updraft itself*, a mechanism examined in previous studies (e.g., Milbrandt and Yau 2005, KR12), and it is well known that maximum hail sizes are strongly correlated with updraft strength. Indeed, the maxima in $D_{mg/h}$ in the supercell experiments are close to the updraft region (see magenta contours in Fig. 5b and Fig. 8 right column), and the updraft determines the initial sizes and distribution of graupel and hail aloft before the particles fall out and advect downstream into the forward flank. Our analysis is instead concerned with the further sorting of graupel and hail once it is advected downstream of the updraft region (outlined by magenta contours in Figs 4-11) into the broad forward flank. Throughout this section, we analyze horizontal cross sections at 700 m AGL through the precipitation shafts, a height at which the Z_{DR} arc in a supercell would be expected to be apparent. For brevity, we will focus on the Z and Z_{DR} fields in the following analysis.

c. Results

We see the same basic patterns in Z, Z_{DR} (Fig. 13), D_{mr}, and D_{mg} (Fig. 14) as in the corresponding full supercell experiments, which lends support to our hypothesis that size sorting graupel/hail is the dominant mechanism modulating the distinct Z_{DR} signatures identified previously, at least in the forward flank region, with additional effects from rain size-sorting. In particular, both 3D3R3HVD and 3D1R3HVD have very similar Z_{DR} signatures (Fig. 13f,h), with the main difference being in the northern third of the precipitation shaft, where 3D1R3HVD has higher Z_{DR} (Fig. 13f) associated with larger D_{mr} (Fig. 14e) than in 3D3R3HVD (Fig. 13h and Fig. 14g, respectively). This difference is due to the lack of size sorting of rain in 3D1R3HVD, and is in agreement with the corresponding results from the supercell experiments discussed previously.

Referring to the rain terminal velocity curve in Fig. 1, one sees that for rain diameters larger than ~4 mm, little change in terminal velocity occurs, and thus limited size sorting of these larger drops will occur, while substantial size sorting of these drops *relative* to drops smaller than ~4 mm will indeed occur. This explains why the high- Z_{DR} region on the southeast flank of the idealized precipitation shaft--where the distribution is dominated by larger drops--in 3D1R3HVD and 3D3R3HVD is so similar, and accordingly why the greatest impact from size sorting on rain occurs in the smaller-drop region in approximately the northern third of the shaft. More specifically, in the area of highest Z_{DR} (> 4.5 dB) centered near the coordinates (22,20) km in Fig. 13,h, the hail is nearly completely melted (not shown) and D_{mh} approaches that of large rain drops (~6-8 mm, Fig. 14f,h). In the same area, D_{mr} is near its maximum allowed size (6 mm, Fig. 14e,g). This juxtaposition of nearly completely melted, small wet hail and large rain drops is what ultimately explains the high Z_{DR} in this region.

Additional insight is gained when we examine the gradients of the mean volume diameter of hail and rain and compare them with the storm-relative mean wind over the entire depth of the precipitation shaft, and over the depth of the sub-melting layer (defined by the wet-bulb zero level of ~ 3 km), respectively. When only hail is allowed to sort (3D1R3HVD, Fig 13,14 third row), the gradients of D_{mh} and D_{mr} align in a similar direction, close to the direction of the mean storm-relative wind vector in the 0.7-12 km layer (magenta vectors in Fig. 14). When instead only rain is allowed to sort (experiment 3D3R1HVD, Fig. 13,14 second row), the gradient in the D_{mr} field (Fig. 14c) aligns more closely with the sub-melting level (0.7-3 km) mean storm relative wind vector (black vectors in Fig. 14). When both hail and rain are allowed to sort (3D3R3HVD, Fig. 13,14 last row), the situation is very similar to 3D1R3HVD, except that the gradient in D_{mr} is shifted slightly toward the direction of 0.7-3 km storm relative mean wind vector (compare Fig. 14g with Fig. 14e). This basic situation is also evident in the full supercell experiments, as can be seen by examining the storm-relative mean wind vectors for the deep (magenta) and shallow (black) for each of the size sorting experiments (Fig. 12). In the supercell simulations, however, perturbations to the environmental wind profile by the storm itself cause these mean wind vectors, and thus the size-sorting pattern, to vary somewhat spatially. Finally, these patterns in D_{mr} and D_{mg} are reflected in an overall slight shift in the higher Z_{DR} toward the downwind (in the deep layer sense) right side of the precipitation shaft for 3D3R3HVD (Fig. 13h), relative to 3D1R3HVD (Fig. 13f).

We also note in the Z_{DR} field for 3D1R3HVD and 3D3R3HVD an area of low Z_{DR} on the upwind side of the precipitation shaft (Fig. 13f,h) that is reflective of the largest D_{mh} and thus PSDs dominated by relatively large and dry hail (Fig. 14f,h). Comparing with the observed storm structure for this case (Fig. 4c), one can see a qualitative agreement in the relative locations and magnitudes of the low-Z_{DR} hail core and the Z_{DR} arc. Finally, it is worth noting again that disabling size sorting for hail substantially degrades the low-level Z_{DR} field as compared with the observations; large and dry hail is not allowed to “sort out”, leading to a muted or absent low-Z_{DR} hail signature in the low levels (Fig. 10,13b,d). We note in passing that this latter result is sometimes observed in tornadic storms (KR08).

5. Summary and Conclusions

This study investigated the impact of size sorting of melting hail and rain in the presence of environmental shear on the qualitative nature of the resulting low level polarimetric fields (with an emphasis on Z_{DR}) in supercell forward flanks through the use of numerical simulation and a sophisticated polarimetric radar emulator operating on the model microphysics state variables. The goals were 1) characterize features in the simulated polarimetric fields, 2) explain the physical cause of these features as a function of size sorting and melting behavior, and 3) broadly compare them with observed features, particularly the Z_{DR} arc or shield commonly observed in the forward flank region of supercell thunderstorms, and the classic low-Z_{DR} hail signature near the storm reflectivity core. The aforementioned goals were accomplished by systematically investigating a series of idealized supercell and simple precipitation shaft simulations using a triple-moment bulk microphysics scheme and varying assumptions about the graupel/hail bulk density and fall speeds, and whether size sorting was allowed in the hail and/or rain fields.

From the results of the numerical experiments, we make the following specific observations and conclusions:

1) The Z_{DR} presentation of simulated supercell forward flanks below the melting level depends strongly on the characteristics of graupel and hail in the model microphysics scheme. In particular, variation of the fall speed and bulk density has a profound effect on the resulting Z_{DR} signatures. When the rimed ice category is more graupel-like, the forward flank region is too broad, gradients in Z_{DR} are weak, and the low-Z_{DR} hail core signature is too expansive, restricting or masking the Z_{DR} arc. However, when the rimed ice category is

more hail-like, the Z_{DR} arc and a low-Z_{DR} hail core that is much closer to the observations in size, magnitude, and location are produced. The best results are obtained for the full triple-moment scheme with separate graupel and hail categories and predicted bulk density and fall speeds.

2) The low-level Z_{DR} signatures in simulated supercell forward flanks are strongly modulated by sustained size sorting in the presence of environmental wind shear. Although size sorting in both the rain and graupel/hail fields is important, it is the sorting of the graupel and hail fields that has greater impact on simulating both the Z_{DR} arc and hail core. Sorting of the rain field mainly modulates the Z_{DR} magnitudes on the left flank of the (right-moving) supercell. These findings extend the arguments of previous studies investigating the size-sorting mechanism in the development of the Z_{DR} arc by implicating sorting of hail and graupel over that of rain.

3) The idealized 3D sedimentation experiments revealed the same trends as the supercell size-sorting simulations. In addition they revealed that the direction of the gradient in mean volume diameter of hail (D_{mh}) and rain (D_{mr}) in the precipitation shafts in this study closely aligned with the average storm-relative wind taken over a deep (~0.7-12 km) layer when only hail is allowed to sort. In contrast, when only rain is allowed to sort, the gradient in D_{mr} aligns most closely with the mean storm-relative wind in the shallow sub-melting (~0.7-3 km) layer, consistent with KR09 (see their Fig. 15). When both hail and rain are allowed to sort, the direction of the D_{mr} gradient is intermediate between the above two situations, but biased toward the deep-layer storm-relative mean

wind. This suggests that a qualitative picture of the near-storm storm-relative wind profile can be achieved by hydrometeor mean diameters estimated from polarimetric variables.

4) The simulated K_{DP} field is qualitatively unaffected by size-sorting, consistent with its known sensitivity to the total amount of liquid water present in a radar volume but not as much (relatively speaking) to the PSD or to the presence of hail. In contrast, regions of simulated $\rho_{HV} < 1$ are strongly tied to the presence of graupel or hail mixed with rain. For the bulk of the simulations that predict only one rimed ice category the best qualitative agreement with the observations results when the category is more hail-like, as was the case with the Z_{DR} field, but the overall predicted magnitudes are too high in the hail core region. Results are improved when two rimed ice categories are predicted, and the additional predicted hydrometeor diversity drives ρ_{HV} values down to values closer to the observations.

5) The sorting of smaller [O(5-10 mm)] hailstones toward the left flank of the (right-moving) supercell and their subsequent melting into large raindrops can produce a secondary region of enhanced Z_{DR} separate from the traditional "Z_{DR} arc". This feature has been tentatively identified in the subject supercell of the current study (the 1 June 2008 storm), and may be present in others as well.

Based on these conclusions, we propose a conceptual model encapsulating the basic physics of the Z_{DR} signatures in the low-levels of supercell thunderstorm forward flanks, which is shown in Fig. 15. The relative degree of size sorting in the hail and rain fields at a given height depends strongly on the wind shear above that height over the depth of the falling precipitation.

In addition, the direction of the horizontal gradient in the mean-volume diameter of hail and rain at a given height appears to be related to the direction of the storm relative wind vector averaged over the depth of the precipitation shaft above that height, but more work needs to be done to quantify this relationship. A similar argument was made regarding the orientation of the Z_{DR} arc in KR09. Thus the relative location of the largest hail in a supercell and the total amount of sorting may be at least partially determined by the magnitude and direction of the deep-layer storm-relative mean winds. We again note that in some cases, the hail signature in the low-levels may be muted or not present (KR08) due to complete melting of hail.

These conclusions on the impact of size sorting on the PSD characteristics of rain and hail would be worth testing for more supercell environments, and bin models of melting hail would be particularly useful for evaluating the bulk model results. The study raises other outstanding questions such as 1) how important is the storm updraft and storm-induced perturbations to the near-storm wind shear (i.e., near the mesocyclone) in affecting the PSD of hail and rain near that feature, as opposed to the preexisting environmental wind shear, 2) can a quantitative relationship between the modeled PSD gradients (such as quantified by mean-volume diameter and shape parameter in the case of the gamma distribution) and the storm relative environmental winds be found and how useful might this information be in diagnosing near-storm wind profiles, and 3) how do these effects feed back to the overall thermodynamic and dynamic structure of the storm, such as the cold pool structure and strength, and tornadic activity?

Appendix A: Description of updated microphysics scheme.

The multimoment microphysics scheme (MZB10) uses a general gamma size distribution (Cohard and Pinty 2000; MY05a; Seifert and Beheng 2006):

$$N_{T,x} \frac{3\mu_x}{\Gamma(\alpha_x+1)} \lambda_x^{(\alpha_x+1)3\mu_x} D_x^{(\alpha_x+1)3\mu_x-1} exp[-(\lambda_x D_x)^{3\mu_x}], \quad \text{(A1)}$$

where α and μ are the first and second shape parameters, $N_{T,x}$ is the particle total number concentration, and the slope parameter λ_x can be defined from the zeroth and third moments of the distribution as

$$\lambda_x = \left[\frac{\pi(\alpha_x+1)}{6\upsilon_0}\right]^{1/3} \text{for } \mu_x = 1, \quad \text{(A2)}$$

$$\lambda_x = \left[\frac{\pi(\alpha_x+3)(\alpha_x+2)(\alpha_x+1)}{6\upsilon_0}\right]^{1/3} \text{for } \mu_x = 1/3, \quad \text{(A3)}$$

where υ_0 is the mean particle volume:

$$\upsilon_0 = \frac{\rho_a q_x}{\rho_x N_{T,x}}, \quad \text{(A4)}$$

Microphysical interactions are described by MZB10. The model was updated with the more general warm-rain equations of Cohard and Pinty (2000) to allow a choice for rain to use the original gamma of volume ($\mu_r = 1$) or a gamma of diameter ($\mu_r = 1/3$). The current results use $\mu_r = 1/3$. The calculation of sixth moment (reflectivity) tendencies follows MY05b, with an addition tendency for graupel and hail. Graupel and hail may have predicted mean particle density, which in turn affects the reflectivity moment via the relationship

$$Z_x = \frac{G(\alpha)}{c_x^2} \frac{(\rho_a q_x)^2}{N_{T,x}}, \quad \text{(A5)}$$

where c_x is the coefficient of the mass-diameter relationship $m_x(D) = c_x D^{d_x}$. For graupel and hail, d_x = 3, and $c_x = (\frac{\pi}{6})\rho_x$. Graupel and hail use $\mu_x = 1/3$, for which $G(\alpha)$ is

$$G(\alpha) = \frac{(6+\alpha)(5+\alpha)(4+\alpha)}{(3+\alpha)(2+\alpha)(1+\alpha)}, \quad \text{(A6)}$$

Following MY05b, Eq. A5 can be differentiated with respect to q_x, $N_{T,x}$, and additionally to c_x for some process *A*:

$$\left.\frac{dZ_x}{dt}\right|_A = G(\alpha)\rho_a^2\left[2\frac{q_x}{N_{T,x}c_x^2}\left.\frac{dq_x}{dt}\right|_A - \left(\frac{q_x}{N_{T,x}c_x}\right)^2\left.\frac{dN_{T,x}}{dt}\right|_A - 2\frac{q_x^2}{N_{T,x}c_x^3}\left.\frac{dc_x}{dt}\right|_A\right], \quad \text{(A7)}$$

The microphysical processes actually adjust the particle volume ($V_x = \rho_a q_x/\rho_x$), so rather than adjust Z_x for each process that affects particle density, a net change in density is calculated as

$$\frac{dc_x}{dt} = \frac{\pi}{6}\frac{d\rho_x}{dt} = \frac{\pi}{6}\frac{\rho_x(t_0+\Delta t)-\rho_x(t_0)}{\Delta t}, \quad \text{(A8)}$$

$$\rho_x(t_0) = \frac{\rho_a q_x(t_0)}{V_x(t_0)}, \quad \text{(A9)}$$

$$\rho_x(t_0+\Delta t) = \frac{\rho_a[q_x(t_0)+\Delta q]}{[V_x(t_0)+\Delta V]}, \quad \text{(A10)}$$

where Δq and ΔV are the net changes to mass mixing ratio and particle volume (Mansell and Ziegler 2013). The density ρ_x is limited within the allowed range $\rho_{x,min}$ to $\rho_{x,max}$ for the particle type.

Acknowledgement: This work was primarily supported by the National Research Council and National Science Foundation Postdoctoral Fellowships (AGS-1137702) awarded to the first author, the NOAA National Severe Storms Laboratory, and was partially supported by NOAA/OAR under NOAA-University of Oklahoma Cooperative Agreement NA11OAR4320072, and NSF grant AGS-1046171. We acknowledge Terry Schuur and other NSSL engineers and scientists who maintain and operate the KOUN polarimetric radar for providing high-quality data. We thank Patrick Marsh for providing portions of the python code used in the analysis. We thank Drs. George Bryan, Hugh Morrison, David Dowell, Glen Romine, and Robin Tanamachi for helpful comments and discussions on earlier versions of this work, and to the anonymous reviewers whose reviews significantly improved the manuscript. Graphics were generated using Matplotlib (Hunter 2007).

References

Balakrishnan, N., and D. S. Zrnic, 1990: Use of polarization to characterize precipitation and discriminate large hail. *J. Atmos. Sci.*, **47,** 152-51540.

Borowska, L., A. Ryzhkov, D. Zrniƒá, C. Simmer, and R. Palmer, 2010: Attenuation and differential attenuation of 5-cm-wavelength radiation in melting hail. *J. Appl. Meteor. Climatol.*, **50,** 59-76.

Bringi, V. N., and V. Chandrasekar, 2001: *Polarimetric Doppler Weather Radar.* Cambridge, 636 pp.

Bringi, V. N., T. Tang, and V. Chandrasekar, 2004: Evaluation of a new polarimetrically based Z-R relation. *Journal of Atmospheric and Oceanic Technology*, **21,** 612-623.

Cohard, J.-M., and J.-P. Pinty, 2000: A comprehensive two-moment warm microphysical bulk scheme. I: Description and tests. *Q. J. Roy. Meteor. Soc*, **126,** 1815-1842.

Dawson, D. T., M. Xue, J. A. Milbrandt, and M. K. Yau, 2010: Comparison of evaporation and cold pool development between single-moment and multimoment bulk microphysics schemes in idealized simulations of tornadic thunderstorms. *Mon. Wea. Rev.*, **138,** 1152-1171.

Ferrier, B. S., 1994: A double-moment multiple-phase four-class bulk ice scheme. Part I: Description. *J. Atmos. Sci.*, **51,** 249-280.

Giangrande, S. E., and A. V. Ryzhkov, 2008: Estimation of rainfall based on the results of polarimetric echo classification. *J. Appl. Meteor. Climatol.*, **47,** 2445-2462.

Gilmore, M. S., J. M. Straka, and E. N. Rasmussen, 2004: Precipitation uncertainty due to variations in precipitation particle parameters within a simple microphysics scheme. *Mon. Wea. Rev.*, **132,** 2610-2627.

Gourley, J. J., P. Tabary, and J. Parent du Chatelet, 2007: A fuzzy logic algorithm for the separation of precipitating from nonprecipitating echoes using polarimetric radar observations. *Journal of Atmospheric and Oceanic Technology*, **24,** 1439-1451.

Heinselman, P. L., and A. V. Ryzhkov, 2006: Validation of polarimetric hail detection. *Wea. Forecasting*, **21,** 839-850.

Herzegh, P. H., and A. R. Jameson, 1992: Oserving precipitation through dual-polarization radar measurements. *Bull. Amer. Meteor. Soc.*, **73,** 1365-1374.

Hunter, J. D., 2007: Matplotlib: A 2D graphics environment. *Computing In Science & Engineering*, **9,** 90-95.

Jung, Y., M. Xue, and G. Zhang, 2010: Simulations of polarimetric radar signatures of a supercell storm using a two-moment bulk microphysics scheme. *J. Appl. Meteor. Climatol.*, **49,** 146-163.

Kumjian, M. R., and A. V. Ryzhkov, 2008: Polarimetric signatures in supercell thunderstorms. *J. Appl. Meteor. Climatol.*, **47,** 1940-1961.

——, 2009: Storm-relative helicity revealed from polarimetric radar measurements. *J. Atmos. Sci.*, **66,** 667-685.

——, 2012: The impact of size sorting on the polarimetric radar variables. *J. Atmos. Sci.*, **69,** 2042-2060.

Kumjian, M. R., A. V. Ryzhkov, V. M. Melnikov, and T. J. Schuur, 2010: Rapid-scan super-resolution observations of a cyclic supercell with a dual-polarization WSR-88D. *Mon. Wea. Rev.*, **138,** 3762-3786.

Mansell, E. R., 2010: On sedimentation and advection in multimoment bulk microphysics. *J. Atmos. Sci.*, **67,** 3084-3094.

Mansell, E. R., and C. L. Ziegler, 2013: Aerosol effects on simulated storm electrification and precipitation in a two-moment bulk microphysics model. *J. Atmos. Sci*.**,** In press.

Mansell, E. R., C. L. Ziegler, and E. C. Bruning, 2010: Simulated electrification of a small thunderstorm with two-moment bulk microphysics. *J. Atmos. Sci.*, **67,** 171-194.

Milbrandt, J. A., and M. K. Yau, 2005: A multi-moment bulk microphysics parameterization. Part II: A proposed three-moment closure and scheme description. *J. Atmos. Sci.*, **62,** 3065-3081.

——, 2005: A multi-moment bulk microphysics parameterization. Part I: Analysis of the role of the spectral shape parameter. *J. Atmos. Sci.*, **62,** 3051-3064.

Milbrandt, J. A., and R. McTaggart-Cowan, 2010: Sedimentation-induced errors in bulk microphysics schemes. *J. Atmos. Sci.*, **67,** 3931-3948.

Milbrandt, J. A., and H. Morrison, 2013: Prediction of graupel density in a bulk microphysics scheme. *J. Atmos. Sci.*, **70,** 410-429.

Mishchenko, M. I., 2000: Calculation of the amplitude matrix for a nonspherical particle in a fixed orientation. *Appl. Opt.*, **39,** 1026-1031.

Naylor, J., and M. S. Gilmore, 2012: Convective initiation in an idealized cloud model using an updraft nudging technique. *Mon. Wea. Rev.*, **140,** 3699-3705.

Park, H. S., A. V. Ryzhkov, D. S. Zrnić, and K.-E. Kim, 2009: The hydrometeor classification algorithm for the polarimetric WSR-88D: description and application to an MCS. *Wea. Forecasting*, **24,** 730-748.

Rasmussen, R. M., and A. J. Heymsfield, 1987: Melting and shedding of graupel and hail. Part I: Model physics. *J. Atmos. Sci.*, **44,** 2754-2763.

Rasmussen, R. M., V. Levizzani, and H. R. Pruppacher, 1984: A wind tunnel and theoretical study on the melting behavior of atmospheric ice particles: III. Experiment and theory for spherical ice particles of radius > 500 μm. *J. Atmos. Sci.*, **41,** 381-388.

Romine, G. S., D. W. Burgess, and R. B. Wilhelmson, 2008: A dual-polarization-radar-based assessment of the 8 May 2003 Oklahoma City area tornadic supercell. *Mon. Wea. Rev.*, **136,** 2849-2870.

Ryzhkov, A., M. Pinsky, A. Pokrovsky, and A. Khain, 2011: Polarimetric radar observation operator for a cloud model with spectral microphysics. *J. Appl. Meteor. Climatol.*, **50,** 873-894.

Ryzhkov, A. V., and D. S. Zrnic, 1998: Discrimination between rain and snow with a polarimetric radar. *J. Appl. Meteor.*, **37,** 1228-1240.

Ryzhkov, A. V., T. J. Schuur, D. W. Burgess, and D. S. Zrnic, 2005: Polarimetric Tornado Detection. *J. Appl. Meteor.*, **44,** 557-570.

Ryzhkov, A. V., T. J. Schuur, D. W. Burgess, P. L. Heinselman, S. E. Giangrande, and D. S. Zrnic, 2005: The Joint Polarization Experiment: Polarimetric rainfall measurements and hydrometeor classification. *Bull. Amer. Meteor. Soc.*, **86,** 809-824.

Seifert, A., and K. D. Beheng, 2006: A two-moment cloud microphysics parameterization for mixed-phase clouds. Part 1: Model description. *Meteor. Atmos. Phys.*, **92,** 45-66.

Seliga, T. A., and V. N. Bringi, 1976: Potential use of radar differential reflectivity measurements at orthogonal polarizations for measuring precipitation. *J. Appl. Meteor.*, **15,** 59-76.

Straka, J. M., D. S. Zrnic, and A. V. Ryzhkov, 2000: Bulk hydrometeor classification and quantification using polarimetric radar data: Synthesis of relations. *J. Appl. Meteor.*, **39,** 1341-1372.

Tessendorf, S. A., L. J. Miller, K. C. Wiens, and S. A. Rutledge, 2005: The 29 June 2000 supercell observed during STEPS. Part I: Kinematics and microphysics. *J. Atmos. Sci.*, **62,** 4127-4150.

Vivekanandan, J., W. M. Adams, and V. N. Bringi, 1991: Rigorous approach to polarimetric radar modeling of hydrometeor orientation distributions. *J. Appl. Meteor.*, **30,** 1053-1063.

Wacker, U., and A. Seifert, 2001: Evolution of rain water profiles resulting from pure sedimentation: Spectral vs. parameterized description. *Atmos. Res.*, **58,** 19-39.

Waterman, P. C., 1969: Scattering by dielectric obstacles. *Alta Freq.*, **38,** 348-352.

Wisner, C., H. D. Orville, and C. Myers, 1972: A numerical model of a hail-bearing cloud. *J. Atmos. Sci.*, **29,** 1160-1181.

Yussouf, N., E. R. Mansell, L. J. Wicker, D. M. Wheatley, and D. J. Stensrud, 2013: The Ensemble Kalman Filter analyses and forecasts of the 8 May 2003 Oklahoma City tornadic supercell storm using single and double moment microphysics schemes. *Mon. Wea. Rev.***,** In press.

Ziegler, C. L., 1985: Retrieval of thermal and microphysical variables in observed convective storms. Part I: Model development and preliminary testing. *J. Atmos. Sci.*, **42,** 1487-1509.

Zrnic, D. S., A. Ryzhkov, J. Straka, Y. Liu, and J. Vivekanandan, 2001: Testing a procedure for automatic classification of hydrometeor types. *Journal of Atmospheric and Oceanic Technology*, **18,** 892-913.

Zrnić, D. S., and A. V. Ryzhkov, 1999: Polarimetry for weather surveillance radars. *Bull. Amer. Meteor. Soc.*, **80,** 389-406.

List of figures

Fig. 1. Terminal velocity-diameter relations for rain, graupel, and hail, as used in the NFD and NVD schemes. The letter labels are used in the experiment names to indicate which fall speed relation for graupel or hail is assumed for the NFD experiments. For the NVD experiments, the graupel/hail density is allowed to vary between the two curves given by the black dashed lines. 39

Fig. 2. Characteristics of melting hail in the polarimetric emulator: maximum allowed water fraction (thin black line), hail axis ratio r_h at maximum water fraction (thin dashed line), and normalized canting angle distribution width (thick dashed line), as a function of diameter of the melting particle. The ice core density of the melting particle is assumed to be 910 kg m^{-3} for the purposes of the maximum water fraction calculation. Also shown for reference is the axis ratio of raindrops r_r as a function of diameter (thin dotted line; for diameters less than 8 mm, the fully melted hail takes on the axis ratio of the corresponding raindrop) and the assumed fixed dry hail axis ratio of 0.75 (thick black line). 40

Fig. 3. 1 June 2008 nontornadic supercell sounding (RUC point sounding valid at 0100 UTC): (a) Skew-T, and (b) hodograph. The black star on the hodograph indicates the approximate observed storm motion. 41

Fig. 4. Left column: representative radar images of the 1 June 2008 northwest OK nontornadic supercell (0.0° elevation, valid 02:55:43 UTC) from the KOUN dual-polarized radar: a) reflectivity at horizontal polarization (dBZ), c) differential reflectivity (dB), e) specific differential phase (deg km^{-1}), and g) cross-correlation coefficient. Thin magenta contours indicate vertical velocity at ~3 km AGL in 10 m s^{-1} increments, starting at 10 m s^{-1}. For

reference, the 30 dBZ reflectivity contour (black) is overlaid in (b-d). Right column: as in left column but for experiment SC3R3HVD at 4200 s and ~732 m AGL. 42

Fig. 5. As in right column of Fig. 4, but for (a) rain mean volume diameter D_{mr} (mm), (b) hail mean volume diameter D_{mh} (mm), and (c) fraction of liquid water on hail F_{WH}. Thin black contours indicate reflectivity (10 dBZ increment, starting at 10 dBZ). The bold solid (dashed) contour indicates Z_{DR} = 4.5 (2.0) dB. Thin magenta contours indicate vertical velocity at ~3 km AGL in 10 m s^{-1} increments, starting at 10 m s^{-1}. 44

Fig. 6. As in Fig. 4 but for experiment SC3R3GHVD, which includes separate variable density graupel and hail categories. 45

Fig. 7. Reflectivity Z (color fill, dBZ, left column) and Differential reflectivity Z_{DR} (color fill, dB, right column) for (a-b) SC3R3GA, (c-d) SC3R3HB, (e-f) SC3R3GC, and (g-h) SC3R3HD. Reflectivity in 20 dBZ increments, starting at 10 dBZ is overlaid with black contours, and vertical velocity in 10 m s^{-1} increments is overlaid with magenta contours in the right column. Each row is labeled by the corresponding fall speed curve and graupel/hail bulk density used and labeled in Fig. 1. 46

Fig. 8. As in Fig. 7 but for (left column) rain mean volume diameter D_{mr} (color fill, mm), and (right column) graupel/hail mean volume diameter $D_{mg/h}$... 47

Fig. 9. As in Fig. 7 but for fraction of liquid water on graupel/hail $FW_{g/h}$. 48

Fig. 10. As in Fig. 7 but for the SC#R#HVD suite of simulations. The number of sedimentation moments for rain and hail predicted in each experiment is labeled on the left of each row. 49

Fig. 11. As in Fig. 10 but for K_{DP} (left column) and ρ_{HV} (right column). 50

Fig. 12. As in Fig. 10 but for (left column) rain mean volume diameter D_{mr} (color fill, mm) and (right column) hail mean volume diameter D_{mh} (color fill, mm). The 0.7-3 km (black) and 0.7-12 km (magenta) storm-relative mean wind vectors are overlaid in 5 km increments.... 51

Fig. 13. As in Fig. 10 but for the idealized steady 3D sedimentation size-sorting experiments (3D#R#HVD, where the # is the number of sedimentation moments) at 1800 s and 700 m AGL. 52

Fig. 14. As in Fig. 12 but for the 3D#R#HVD experiments. 53

Fig. 15. Schematic summarizing the main conclusions of the study. (a) gradient of rain mean mass diameter from largest (blue) to smallest (white), along with low-level (~1-3 km) storm-relative mean wind vector, (b) gradient of hail mean mass diameter from largest (red) to smallest (white), along with deep-layer (~1-9 km) storm-relative mean wind vector, and (c) corresponding typical Z_{DR} signatures. 54

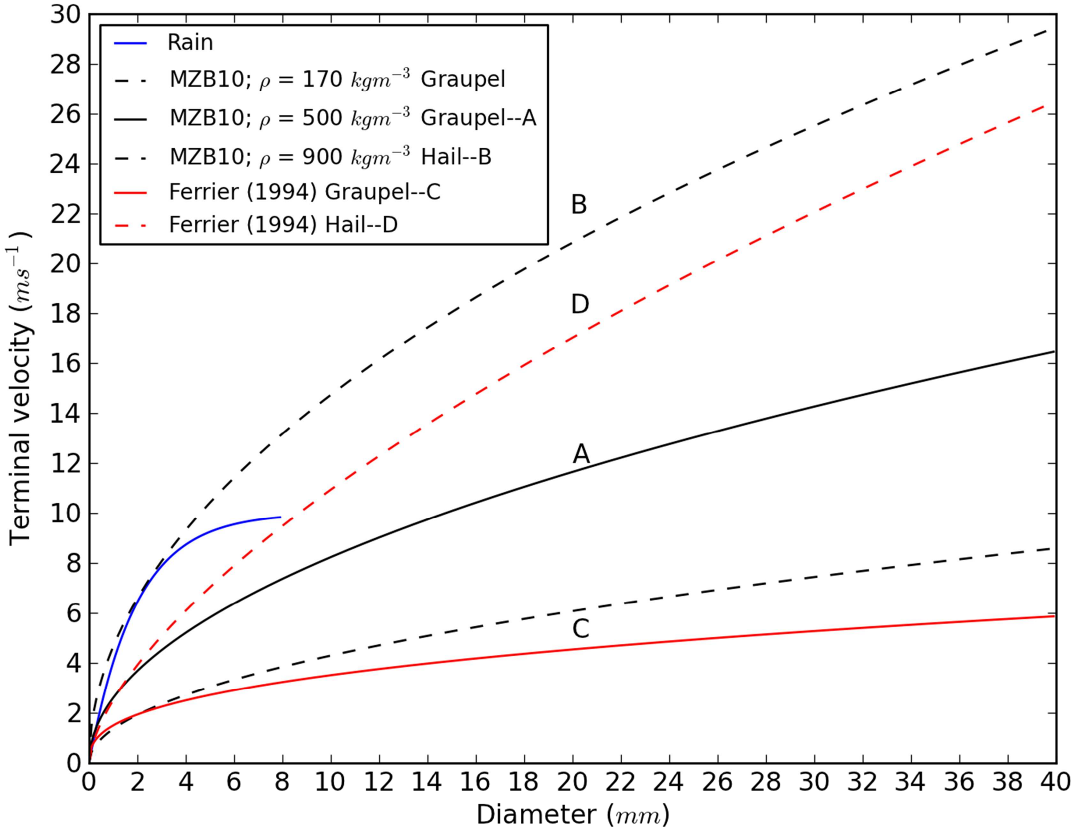

Fig. 1. Terminal velocity-diameter relations for rain, graupel, and hail, as used in the NFD and NVD schemes. The letter labels are used in the experiment names to indicate which fall speed relation for graupel or hail is assumed for the NFD experiments. For the NVD experiments, the graupel/hail density is allowed to vary between the two curves given by the black dashed lines.

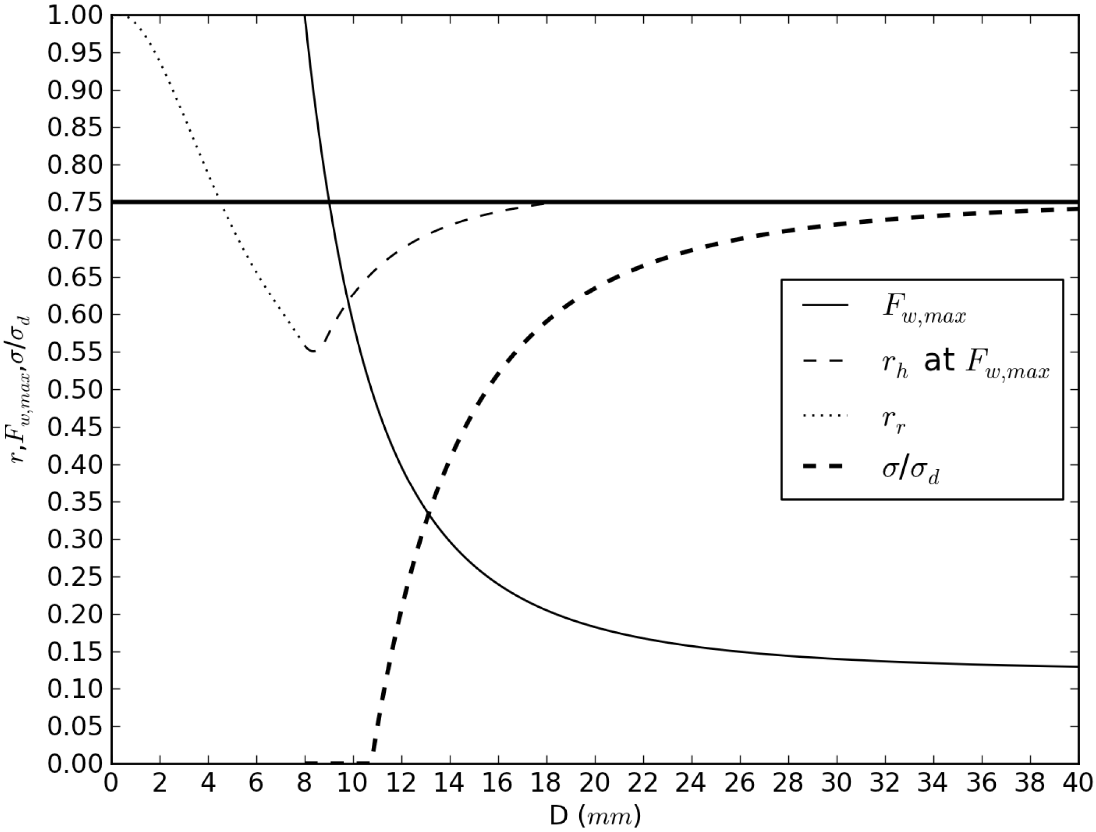

Fig. 2. Characteristics of melting hail in the polarimetric emulator: maximum allowed water fraction (thin black line), hail axis ratio r_h at maximum water fraction (thin dashed line), and normalized canting angle distribution width (thick dashed line), as a function of diameter of the melting particle. The ice core density of the melting particle is assumed to be 910 kg m^{-3} for the purposes of the maximum water fraction calculation. Also shown for reference is the axis ratio of raindrops r_r as a function of diameter (thin dotted line; for diameters less than 8 mm, the fully melted hail takes on the axis ratio of the corresponding raindrop) and the assumed fixed dry hail axis ratio of 0.75 (thick black line).

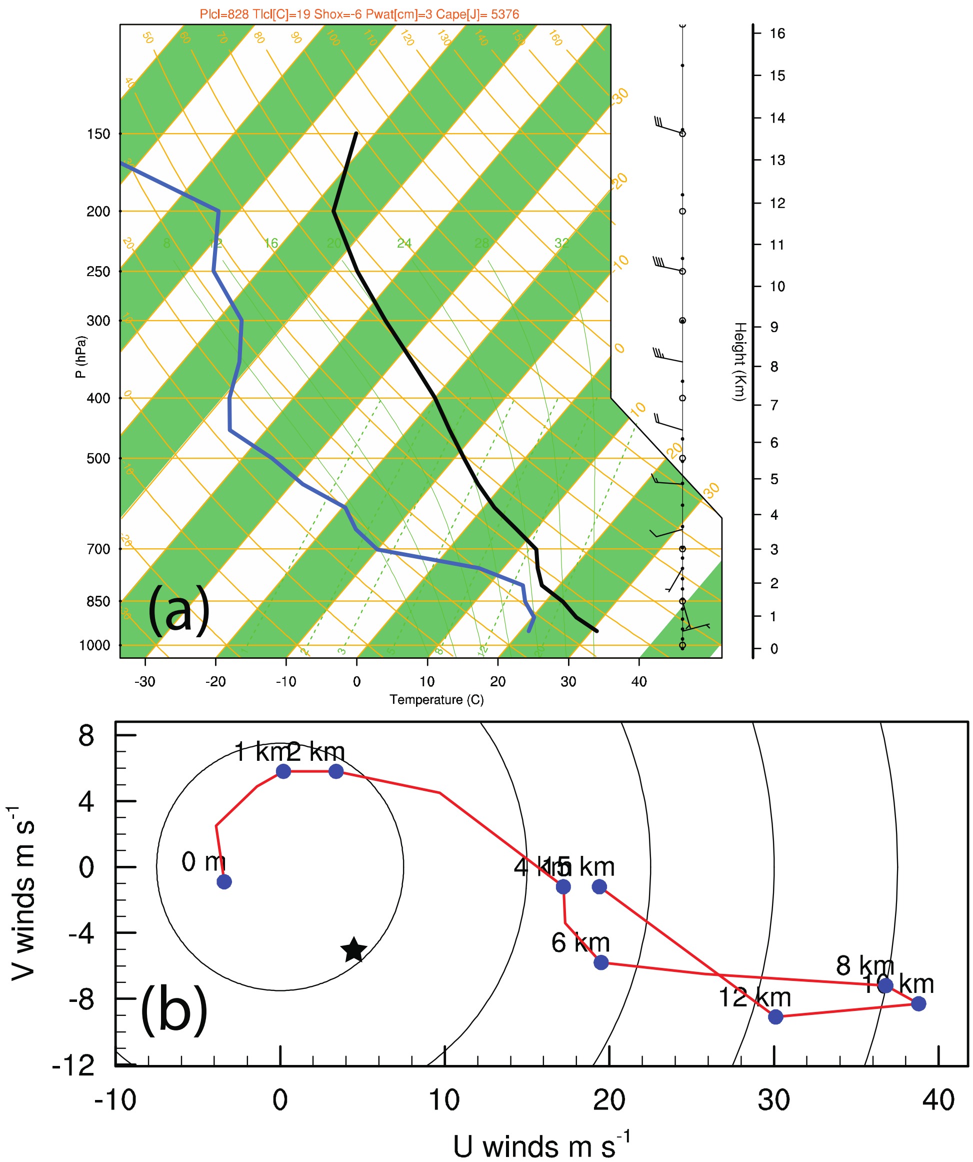

Fig. 3. 1 June 2008 nontornadic supercell sounding (RUC point sounding valid at 0100 UTC): (a) Skew-T, and (b) hodograph. The black star on the hodograph indicates the approximate observed storm motion.

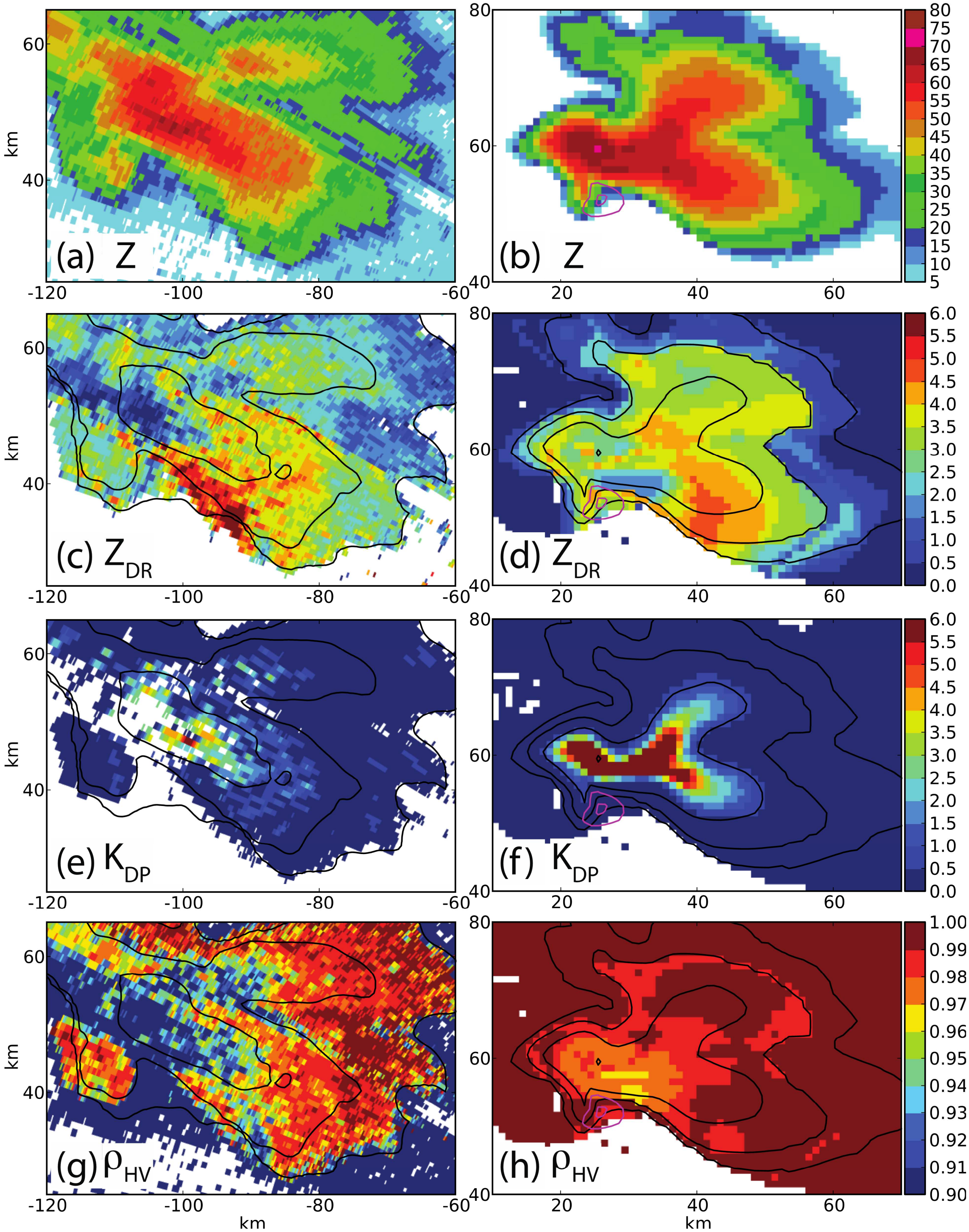

Fig. 4. Left column: representative radar images of the 1 June 2008 northwest OK nontornadic supercell (0.0° elevation, valid 02:55:43 UTC) from the KOUN dual-polarized radar: a) reflectivity at horizontal polarization (dBZ), c) differential reflectivity

(dB), e) specific differential phase (deg km^{-1}), and g) cross-correlation coefficient. Thin magenta contours indicate vertical velocity at ~3 km AGL in 10 m s^{-1} increments, starting at 10 m s^{-1}. For reference, the 30 dBZ reflectivity contour (black) is overlaid in (b-d). Right column: as in left column but for experiment SC3R3HVD at 4200 s and ~732 m AGL.

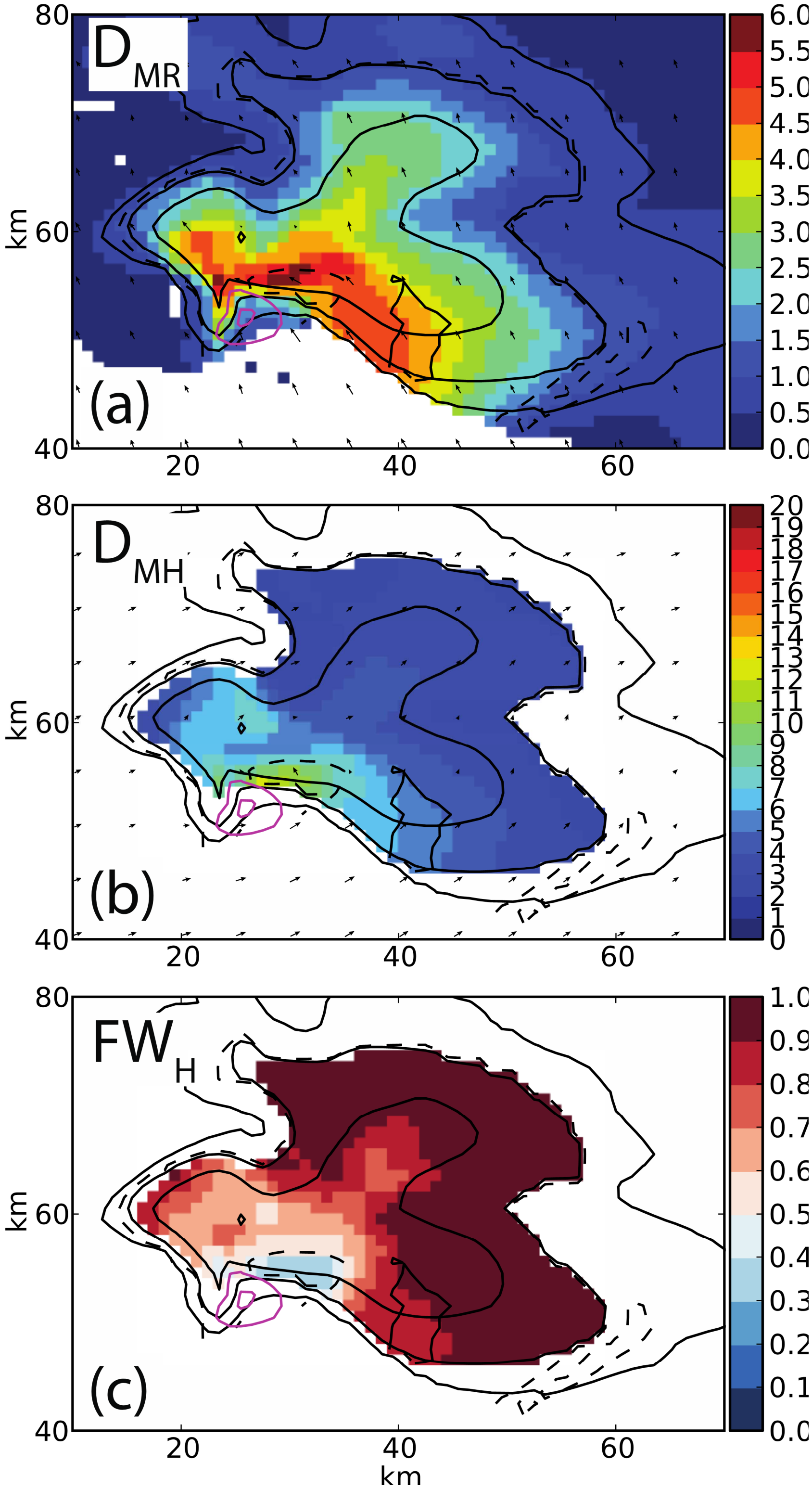

Fig. 5. As in right column of Fig. 4, but for (a) rain mean volume diameter D_{mr} (mm), (b) hail mean volume diameter D_{mh} (mm), and (c) fraction of liquid water on hail F_{WH}. Thin black contours indicate reflectivity (10 dBZ increment, starting at 10 dBZ). The bold solid (dashed) contour indicates Z_{DR} = 4.5 (2.0) dB. Thin magenta contours indicate vertical velocity at ~3 km AGL in 10 m s^{-1} increments, starting at 10 m s^{-1}.

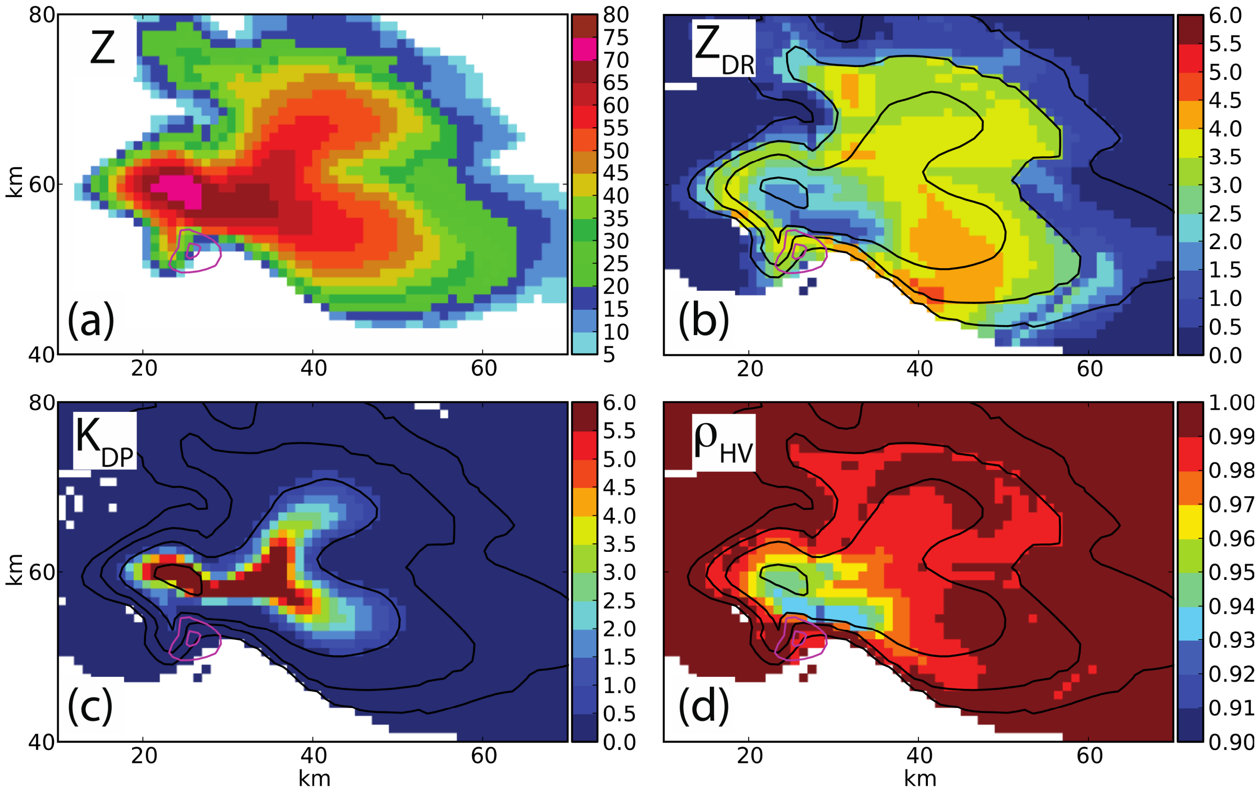

Fig. 6. As in Fig. 4 but for experiment SC3R3GHVD, which includes separate variable density graupel and hail categories.

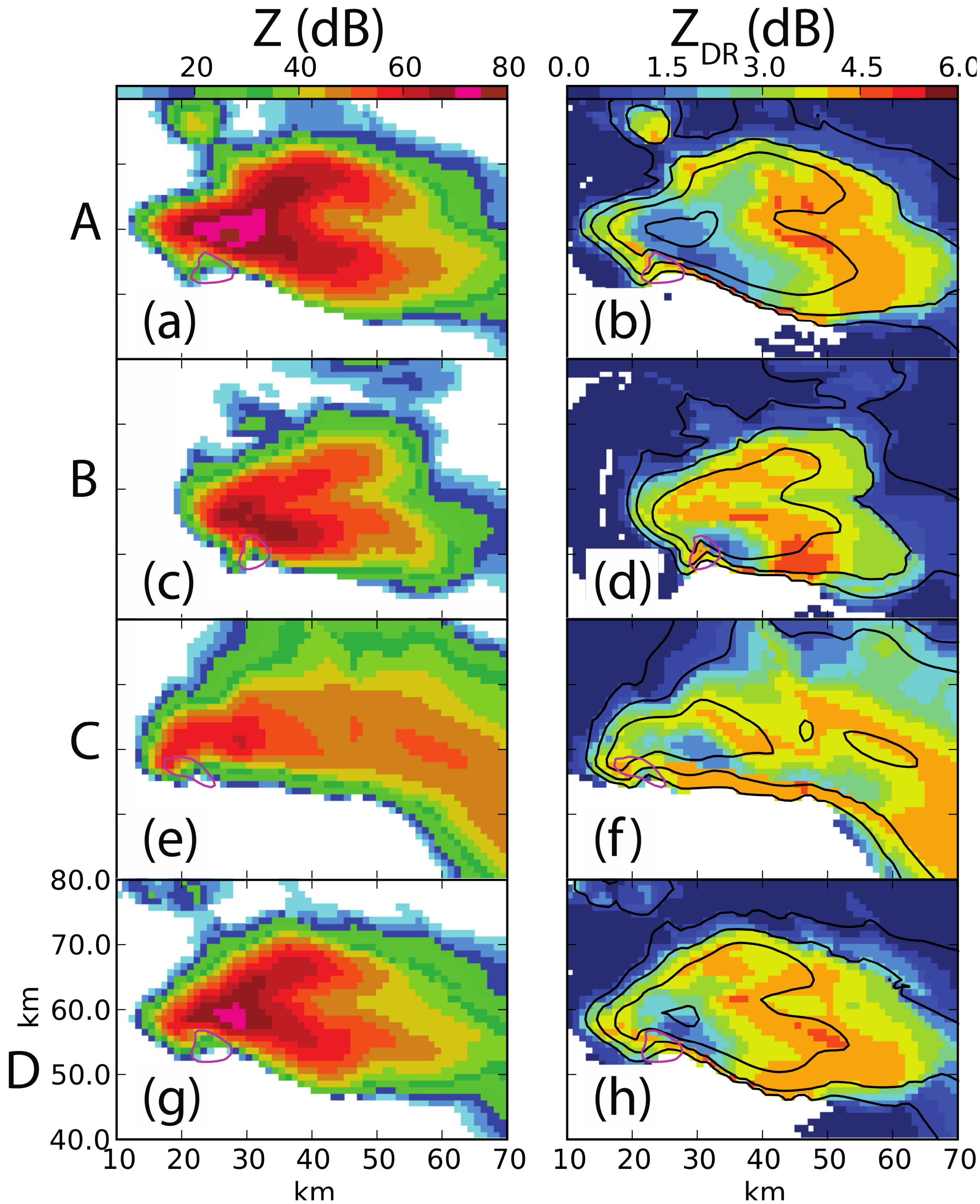

Fig. 7. Reflectivity Z (color fill, dBZ, left column) and Differential reflectivity Z_{DR} (color fill, dB, right column) for (a-b) SC3R3GA, (c-d) SC3R3HB, (e-f) SC3R3GC, and (g-h) SC3R3HD. Reflectivity in 20 dBZ increments, starting at 10 dBZ is overlaid with black contours, and vertical velocity in 10 m s^{-1} increments is overlaid with magenta contours in the right column. Each row is labeled by the corresponding fall speed curve and graupel/hail bulk density used and labeled in Fig. 1.

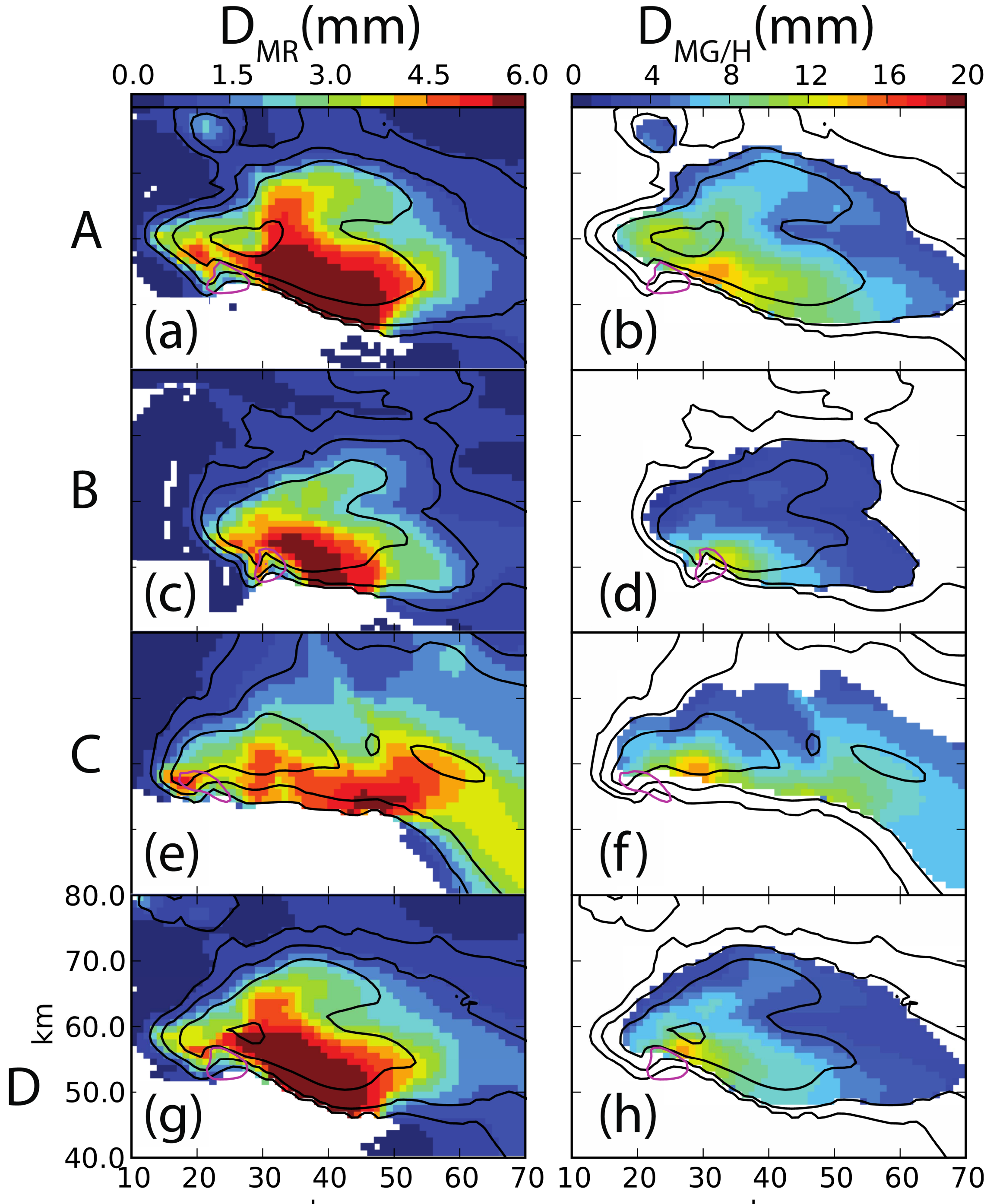

Fig. 8. As in Fig. 7 but for (left column) rain mean volume diameter D_{mr} (color fill, mm), and (right column) graupel/hail mean volume diameter $D_{mg/h}$.

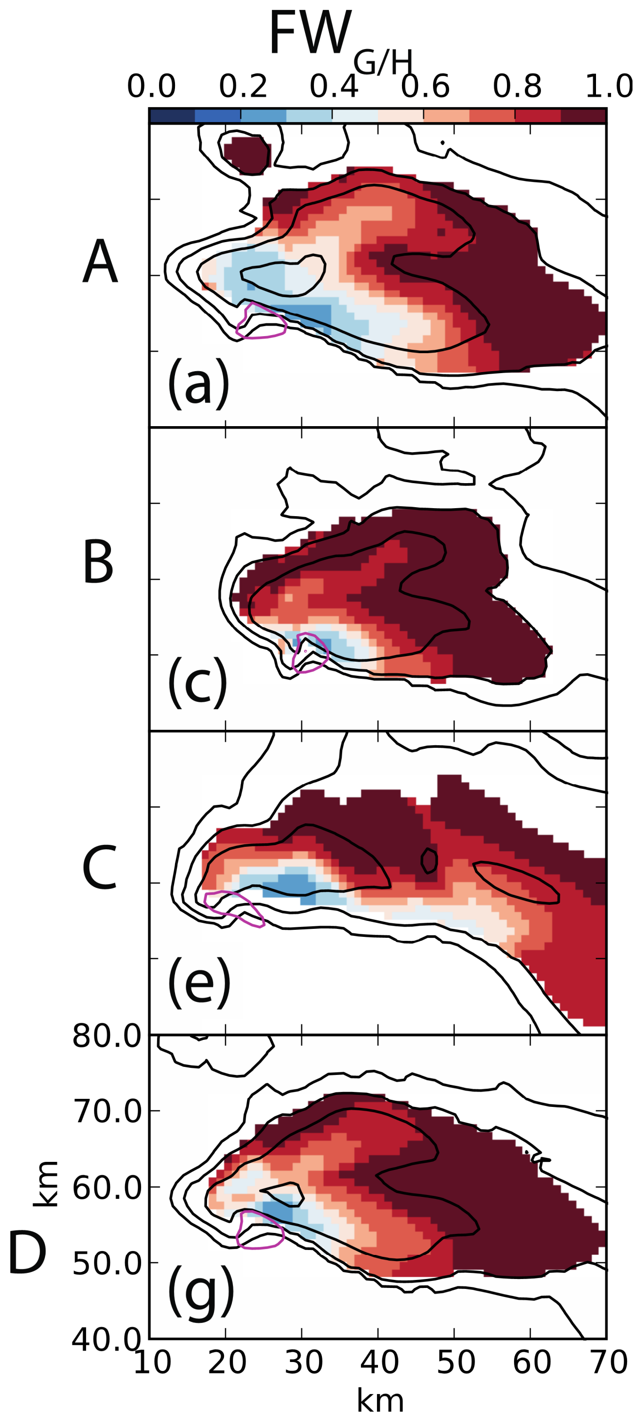

Fig. 9. As in Fig. 7 but for fraction of liquid water on graupel/hail $FW_{g/h}$.

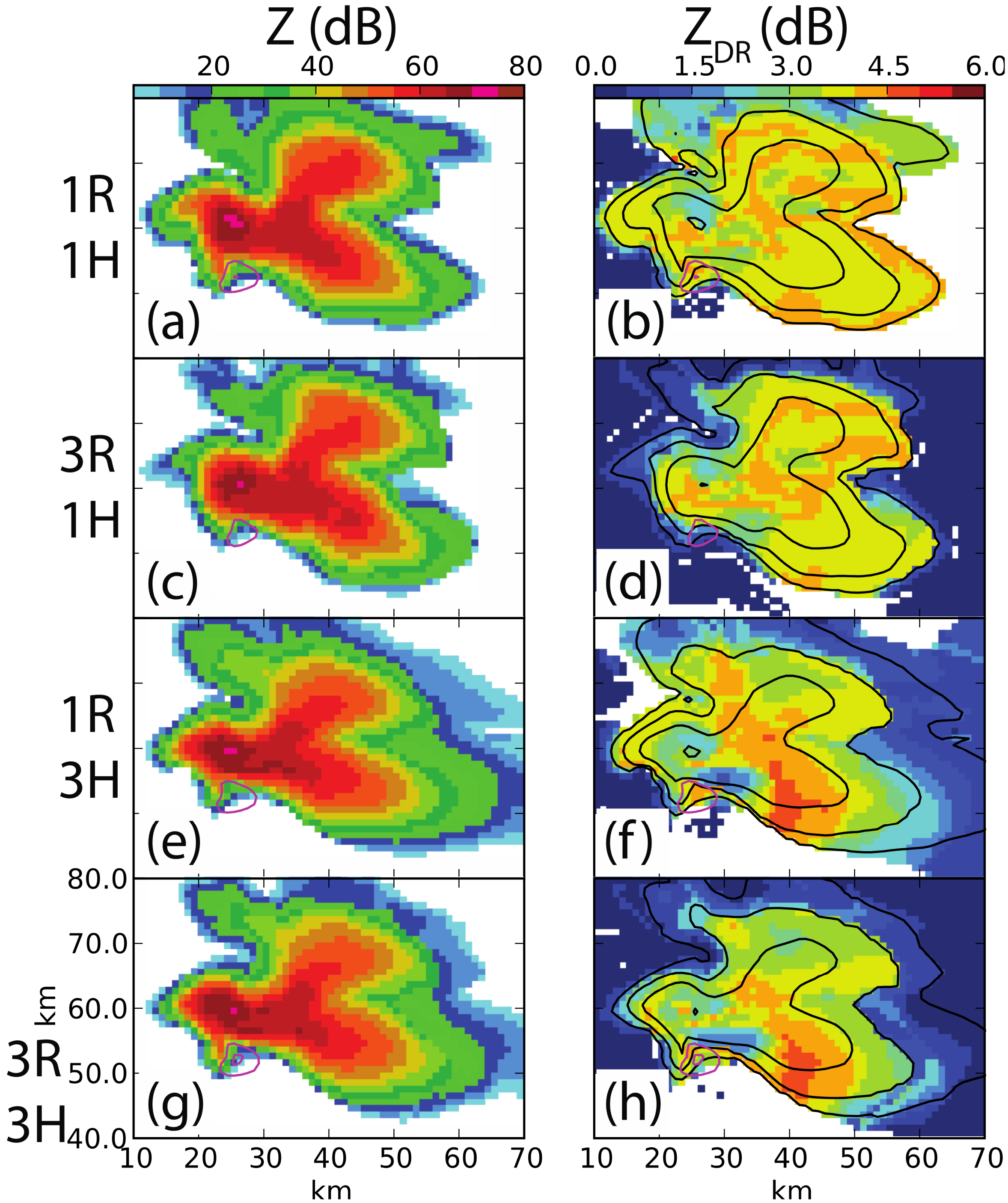

Fig. 10. As in Fig. 7 but for the SC#R#HVD suite of simulations. The number of sedimentation moments for rain and hail predicted in each experiment is labeled on the left of each row.

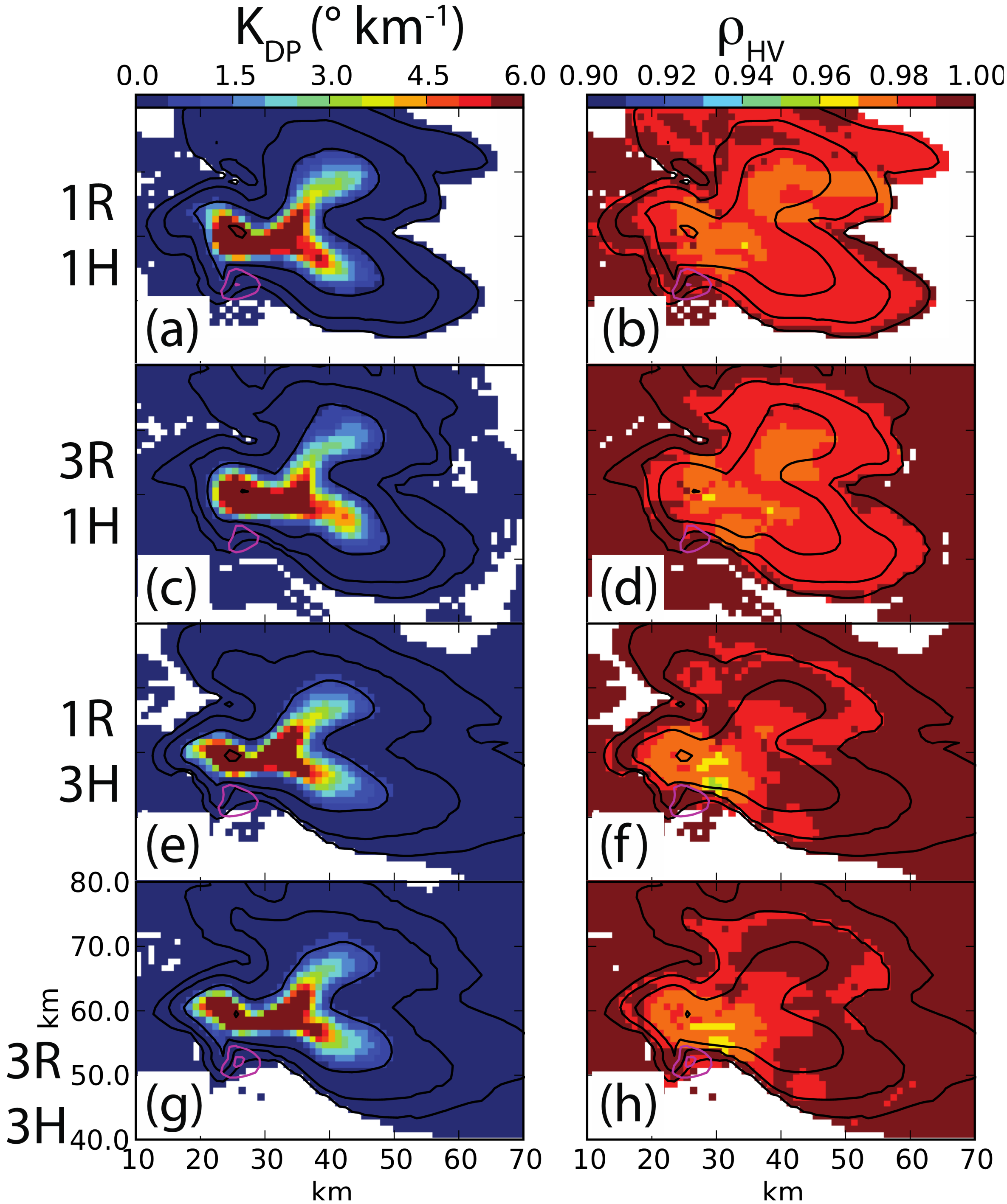

Fig. 11. As in Fig. 10 but for K_{DP} (left column) and ρ_{HV} (right column).

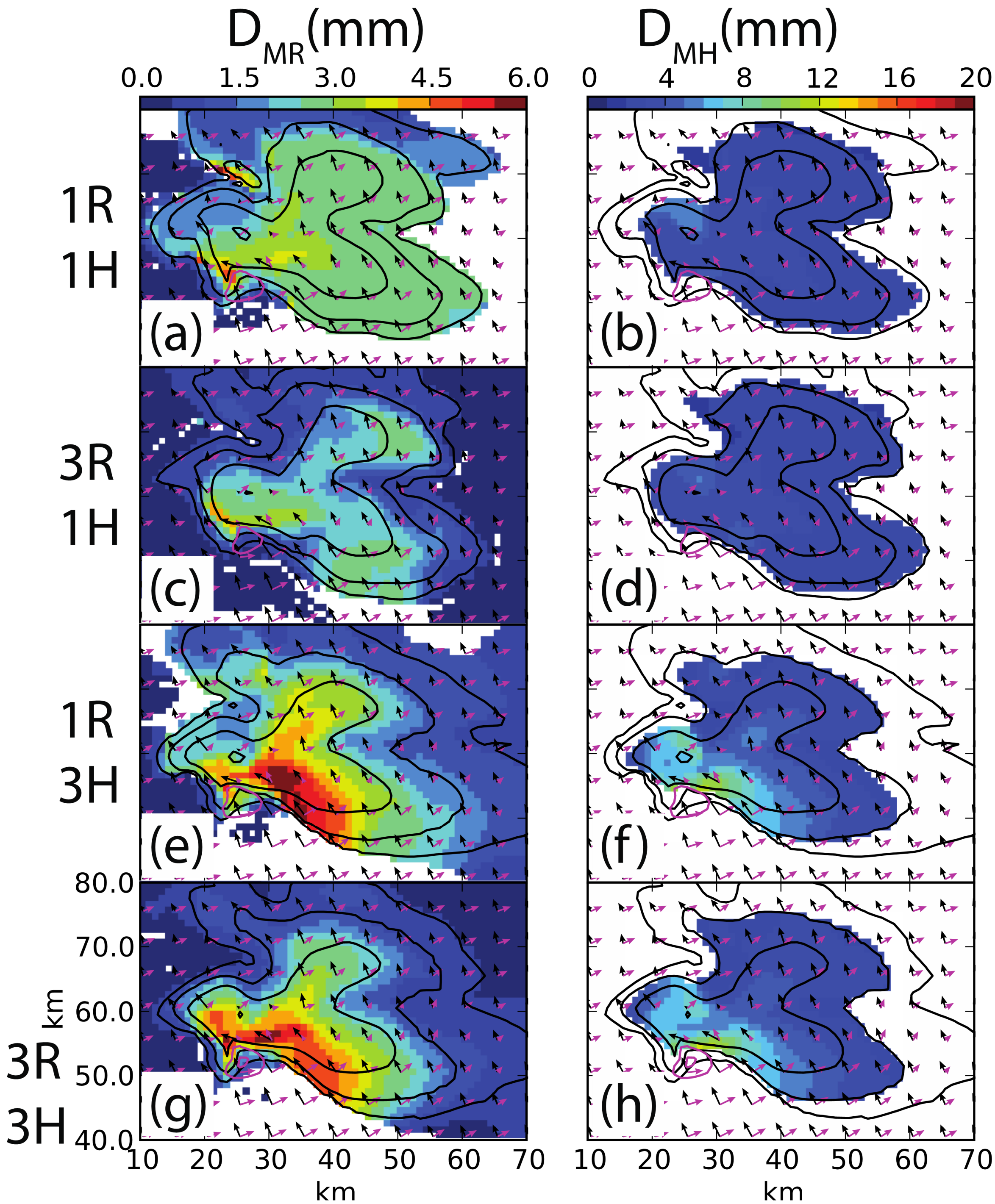

Fig. 12. As in Fig. 10 but for (left column) rain mean volume diameter D_{mr} (color fill, mm) and (right column) hail mean volume diameter D_{mh} (color fill, mm). The 0.7-3 km (black) and 0.7-12 km (magenta) storm-relative mean wind vectors are overlaid in 5 km increments.

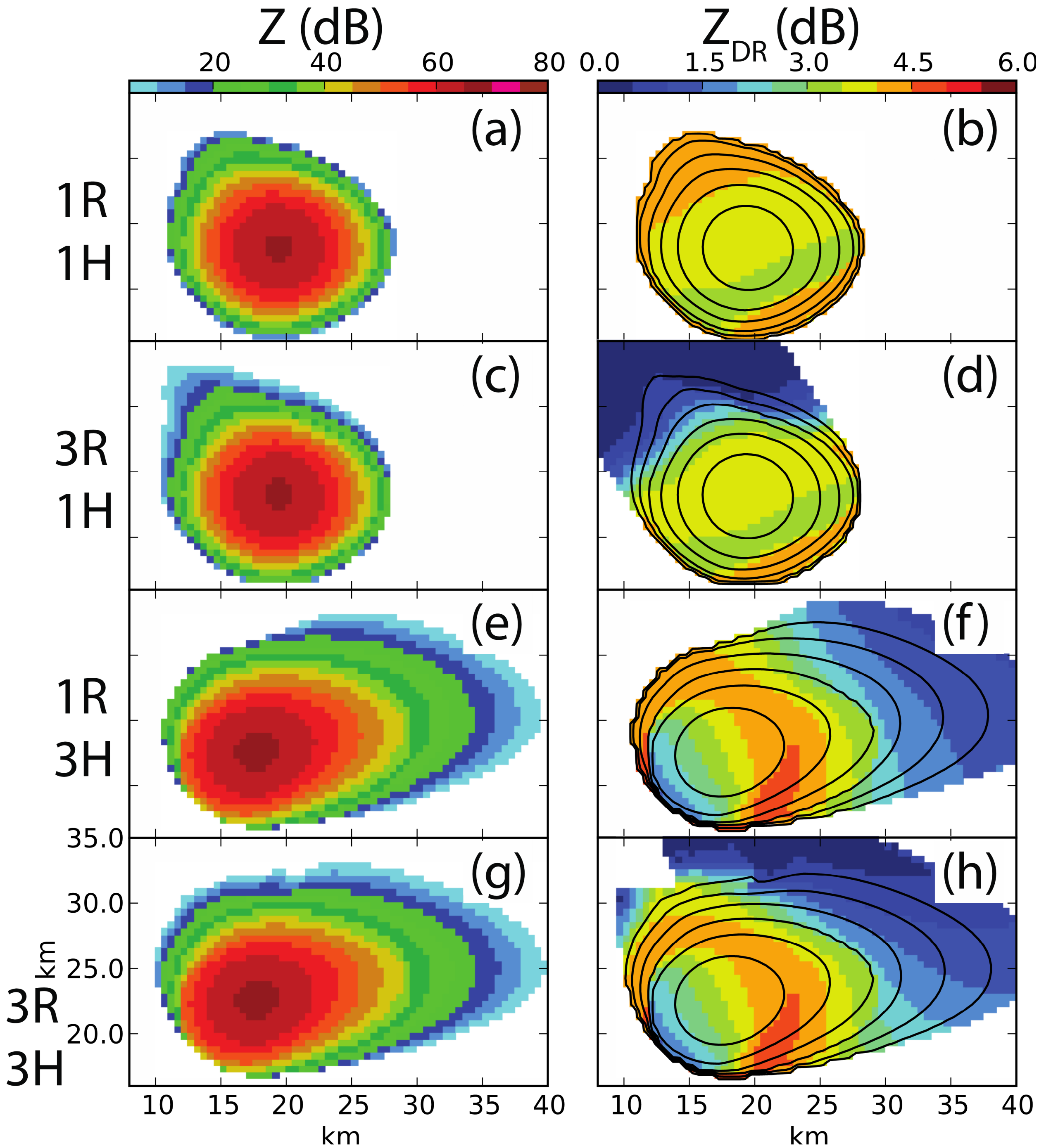

Fig. 13. As in Fig. 10 but for the idealized steady 3D sedimentation size-sorting experiments (3D#R#HVD, where the # is the number of sedimentation moments) at 1800 s and 700 m AGL.

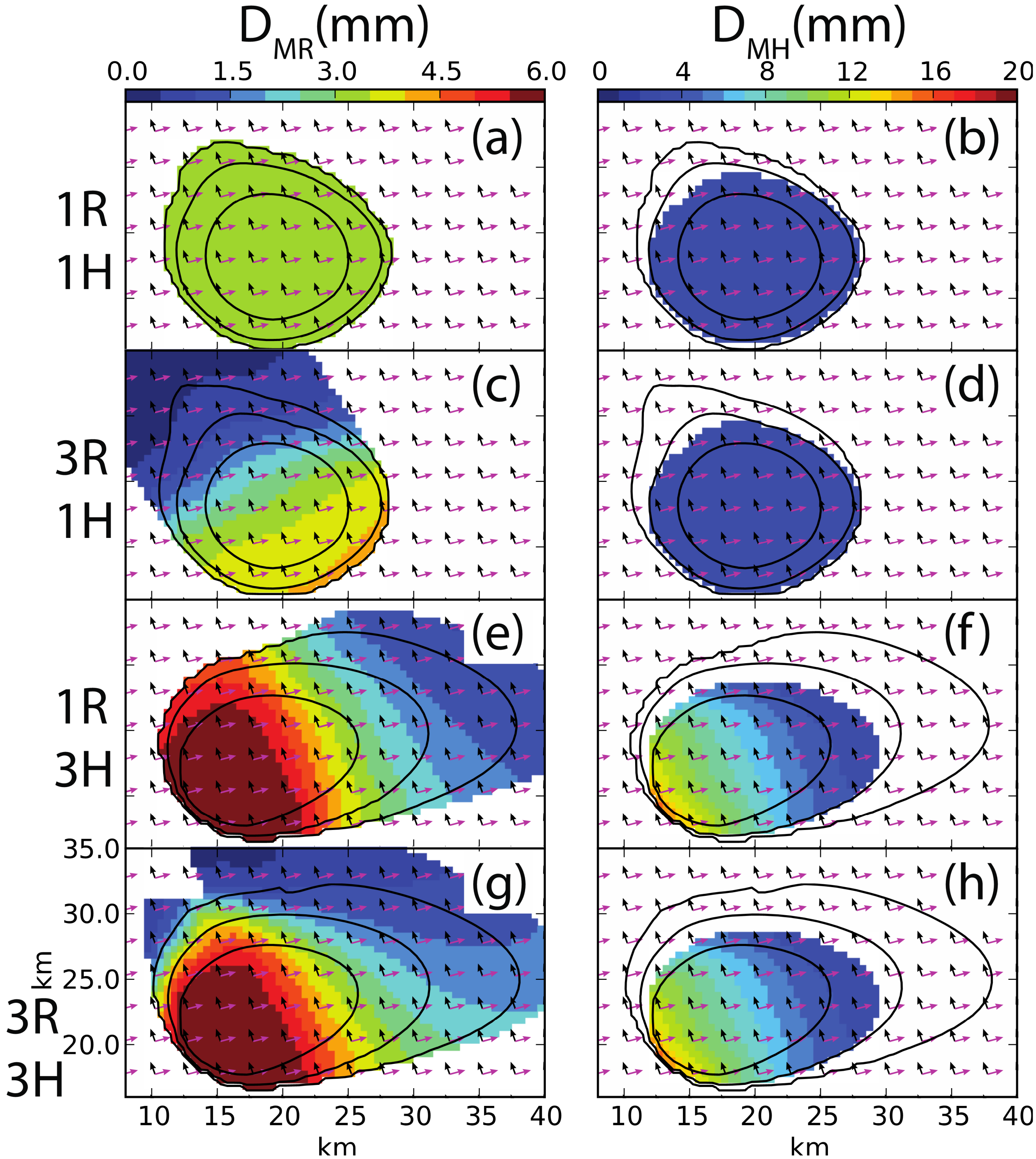

Fig. 14. As in Fig. 12 but for the 3D#R#HVD experiments.

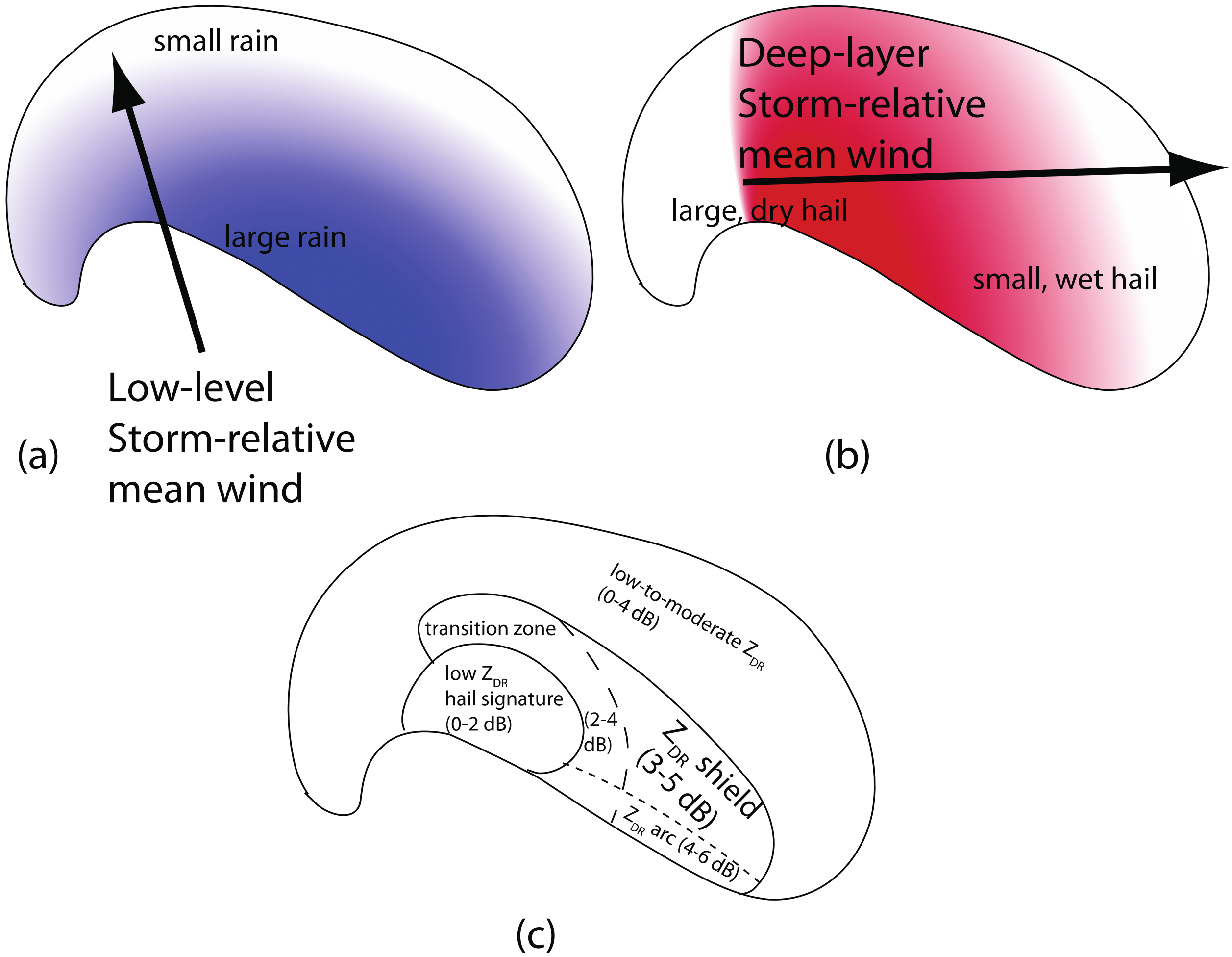

Fig. 15. Schematic summarizing the main conclusions of the study. (a) gradient of rain mean mass diameter from largest (blue) to smallest (white), along with low-level (~1-3 km) storm-relative mean wind vector, (b) gradient of hail mean mass diameter from largest (red) to smallest (white), along with deep-layer (~1-9 km) storm-relative mean wind vector, and (c) corresponding typical Z_{DR} signatures.

Table 1. Summary of fall speed relations for rain, graupel, and hail.

Category	**Fall speed relation**	$\boldsymbol{a_x}$	$\boldsymbol{b_x}$
Rain	$v_{tr} = \gamma a_r(1 - \exp(-b_r D))$	10	516.575
Graupel - A	$v_{tg} = \gamma a_g D^{b_g}$	$a_g = \left(\frac{4\rho_g g}{3C_D\rho_a}\right)$, $C_D = 0.8$	0.5
Hail - B	$v_{th} = \gamma a_h D^{b_h}$	$a_h = \left(\frac{4\rho_h g}{3C_D\rho_a}\right)$, $C_D = 0.45$	0.5
Graupel - C	$v_{tg} = \gamma a_g D^{b_g}$	19.3	0.37
Hail - D	$v_{th} = \gamma a_h D^{b_h}$	206.984	0.6384
Variable density graupel/hail	$v_{tg/h} = \gamma a_{g/h} D^{b_{g/h}}$	$a_{g/h} = \left(\frac{4\rho_h g}{3C_D\rho_a}\right)$, $C_D = 0.45$-1.0, $\rho_{g/h} = 170 - 900$	0.5

Table 2. Summary of supercell experiments using the 1 June 2008 environment shown in Fig. 3. Fall speed/density labels correspond to the labeled curves in Fig. 1

Experiment identifier	**Description**
SC3R3GA	3M rain, 3M graupel; “A” density/fall speed
SC3R3HB	3M rain, 3M hail; “B” density/fall speed
SC3R3GC	3M rain, 3M graupel; “C” density/fall speed
SC3R3HD	3M rain, 3M hail; “D” density/fall speed
SC1R1HVD	1M rain, 1M hail; Variable density/fall speeds
SC1R3HVD	1M rain, 3M hail; Variable density/fall speeds
SC3R1HVD	3M rain, 1M hail; Variable density/fall speeds
SC3R3HVD	3M rain, 3M hail; Variable density/fall speeds
SC3R3GHVD	3M rain, 3M graupel, 3M hail; Variable density/fall speeds

Table 3. Idealized simulation characteristics

Domain size	100 km x 100 km (horizontal), 20 km vertical
Grid spacing	1 km horizontal; stretched from 200 m at the bottom to 500 m at the top in the vertical; 50 vertical levels
Boundary conditions	Open lateral; free slip bottom and top
Time step	4 s (large), 2/3 s (small)
Radiation, surface physics, Coriolis force	None
Subgrid-scale turbulence parameterization	1.5 order prognostic TKE closure
Microphysics	NSSL Variable/Fixed Density Multi-moment scheme (Ziegler et al. 1985, Mansell et al. 2010)
Convective initiation procedure	Updraft nudging (Naylor and Gilmore 2012) to 10 m s^{-1} applied over the first 900 s in an ellipsoidal region (30x30x6km); center placement at 40x40x1.5 km relative to SW corner of domain.

Table 4. As in Table 1 but for the 3D sedimentation experiments.

Experiment identifier	**Description**
3D1R1HVD	1M rain, 1M hail; Variable density/fall speeds
3D1R3HVD	1M rain, 3M hail; Variable density/fall speeds
3D3R1HVD	3M rain, 1M hail; Variable density/fall speeds
3D3R3HVD	3M rain, 3M hail; Variable density/fall speeds